Multiscale modelling and experimental analysis of ultrasonic-assisted drilling of GLARE fibre metal laminates

Muhammad Atif [a], Xibin Wang [a], Lijing Xie [a,*], Khaled Giasin [b,*], Yuan Ma [c,d], Chulin Jiang [e], Ugur Koklu [f], Jos Sinke [g]

[a] Beijing Institute of Technology, 5 Zhongguancun St, Haidian District, Beijing 100811, China
[b] School of Mechanical and Design Engineering, University of Portsmouth, Anglesea Building, Anglesea Rd, Portsmouth, PO1 3DJ, UK
[c] State Key Laboratory of Tribology, Department of Mechanical Engineering, Tsinghua University, Beijing 100084, China
[d] Shenzhen Tsingding Technology Co., Ltd., Shenzhen 518101, China
[e] Teesside University, Campus Heart, Southfield Rd, Middlesbrough TS1 3BX, UK
[f] Karamanoglu Mehmetbey University, Faculty of Engineering, Department of Mechanical Engineering, Turkey
[g] Delft University, Kluyverweg 1, 2629 HS Delft, the Netherlands

A B S T R A C T

This study aims to evaluate the effectiveness of Ultrasonic-assisted drilling (UAD) of Glass laminate aluminium reinforced epoxy (GLARE) at high cutting speeds (Spindle speeds: 3000–7500 rpm; feed rates 300–750 mm/min) by analysing the thrust force and hole quality metrics (surface roughness, hole size, and burr formations). The research also presents numerical modelling of FMLs under conventional and UAD regimes to predict thrust force using ABAQUS/SIMULIA. The thrust force and exit burrs were reduced by up to 40.83 % and 80 %, respectively. The surface roughness metrics (R_a and R_z) were slightly higher using UAD but remained within the desirable limits of surface roughness for machined aeronautical structures. The discrepancy between the simulation and experimental results was adequate and did not exceed 15 %. The current study shows that it is feasible to drill holes in GLARE using higher cutting parameters and maintain excellent hole quality, which means increased productivity and reduced costs.

1. Introduction

Glass laminate aluminium-reinforced epoxy (GLARE) belongs to the family of fibre metal laminates (FML). Because of its exceptional qualities, GLARE is used in aeronautical structural applications. GLARE offers high impact resistance and weight reduction compared to monolithic aluminium alloys [1,2]. GLARE is made from a combination of sheets made from aluminium alloys (mainly Al2024) and unidirectional glass fibre prepregs known as magnesium alumina silicate glasses (S2 glass fibre) [3]. GLARE was mainly developed as an aerospace structure due to its high fatigue resistance and to reduce the weight of structural components. It also has good insulation and damping properties [4]. GLARE was utilized for the first time in the Airbus A380 structure, achieving significant weight reductions compared to aluminium panels [5]. GLARE structures are assembled with other structures in an aircraft using milling (to trim the edges) and drilling (to create holes and install rivets) operations since they provide better

surface quality and dimensional accuracy than other machining processes [1]. Drilling parameters, cutting conditions, coolants, tool, and workpiece properties can affect surface roughness, burr formation, and delamination. Literature also shows that two flute twist drills provide better results than three flute twist drills in terms of burr formation and delamination [6]. Delamination near the hole exit can occur in GLARE laminates if the thrust force exceeds a certain critical level [1]. Drill geometry, feed rate, and cutting speed have the most impact on the thrust force [7]. To better estimate the thrust force for drilling composite material, researchers have created new models that consider the shape of the tool geometry and cutting zone temperature. Unlike homogenous material (metals), GLARE laminates are a combination of both homogenous and non-homogenous materials, which have different properties that makes them susceptible to different kind of defects and more complicated to machine [1]. Drilling GLARE laminates presents several challenges, one of which is burr formation. If significant, it can be removed by a post-machining process (deburring), but this process is

challenging to automate and time-consuming [8]. It accounts for around 40 % of the total manufacturing time [9,10]. Reducing burr formation during the drilling process is also crucial as it affects the surface roughness [11]. The influence of drilling parameters on thrust force is the same for GLARE as that of other metals and is not affected by fibre orientation. According to the findings, an increase in the feed rate and a decrease in the spindle speed were observed to increase the thrust force [12]. Less damage was observed around the hole when using a lower cutting speed of 1000 rpm, possibly due to the lower cutting temperatures [13]. It was also reported that drilling holes with a higher feed rate and spindle speed resulted in a poor surface finish [14]. Delamination in GLARE is almost negligible compared to that formed when drilling composites due to the stacking nature of the laminate [14]. The metal sheets function as a backup plate, reducing the likelihood of delamination and deformations around the hole edge at entrance and exit. The tool coating was also found to be an influencing factor in increasing the hole dimensional accuracy [12]. A high feed rate was found unsuitable for drilling of GLARE laminate as it increases the tool vibration and defection in the workpiece, causing an increase in circularity error [15]. Recently, a newer helical milling process was employed to drill holes in GLARE laminate, chip evacuation was improved compared to conventional drilling due to the production of powdery discontinuous chips [16]. Cutting temperature is an essential parameter in ensuring the reduction of thermal degradation. While drilling GLARE, the lower temperature was produced at high spindle speed and feed rate, which helps reduce the thermal degradation of the matrix [17].

The use of UAD has risen over the last several decades, in which the vibration is isolated in the feed direction to help with chip evacuation and reduce cutting time by decreasing tool-to-workpiece contact. In the vibrational drilling of composites, the vibration amplitude is kept higher than the feed/tooth which is more time-consuming because of its low feed rate but still considered superior to the normal drilling process [18]. LVAD (Low vibration assisted drilling) was used for CFRP (Carbon fibre reinforced polymer) drilling with constant and hybrid variation parameters. For the hybrid variation parameters LVAD, the efficiency was increased up to 52.1 % compared to the conventional drilling CD process in terms of delamination at optimal cutting conditions [19]. Experiments were also performed on high amplitude and low frequency which almost doubled the tool life compared to CD thanks to improved chip-breakability, reduction in cutting forces, and lower tool-to-workpiece contact [20]. Comparing low-frequency VAD to CD, a reduction in the delamination factor by 5 % to 11 % was achieved [18]. Additionally, UAD demonstrated a substantial delamination reduction of up to 50 %, accompanied by decreased burr formation and improved surface roughness in comparison to CD [21–23]. The use of UAD was shown to be more efficient in lowering thrust force for metals with higher strength such as Ti-6Al-4 V than softer ones such as Al2024-T3 [24]. The surface roughness and hole geometry were found to improve by increasing the vibration amplitude [25]. It was also found that the thrust force, surface roughness, cutting temperature, delamination, and hole size were reduced using UAD compared to CD when drilling composites and metals [26–28]. Cheng et al. [29] investigated the Ultrasonic Assisted Machining (UAM) of titanium alloy using Finite Element Analysis (FEA). Their findings indicated that augmenting the amplitude and frequency of vibrations along the x-direction (feed direction) led to a reduction in cutting forces, with a relatively minor impact on plastic dissipation energy. Conversely, when these factors were increased along the y-direction (perpendicular to the feed), a notable rise in plastic dissipation energy and cutting forces was observed. The decrease in forces is due to the increase in heat, which causes the thermal softening of the workpiece. The increase in vibration amplitude, stress, equivalent plastic strain, and temperature concentration help in forming serrated chips. The UAD process requires special equipment that is expensive and time-consuming, which makes it difficult to find the best cutting parameters using the hit-and-trial method [30]. An alternative method is required with low cost and complication

to overcome these problems. FEA is an alternative method that can be used to predict different aspects of the machining process. Some of the first work on the FEA of UAD on composites was done by Phadnis et al. [31,32], during which they predicted the cutting forces. The cutting forces produced during the UAD were 30 % lower than in conventional drilling (CD).

The research efforts of H. Hocheng et al. [33,34] and P. Rahme et al. [35,36], systematically address the pivotal challenge of delamination in fibre-reinforced composite materials during drilling processes. Hocheng's work emphasizes innovative strategies such as specialized drill bits, step drilling, and non-traditional methods to circumvent delamination risks, accompanied by insightful analyses of the thrust force and practical tool application. Similarly, Rahme's investigations concentrate on counteracting delamination by introducing a woven glass ply and optimizing drilling conditions using a step gun drill. Collectively, these studies contribute valuable insights into minimizing delamination, enhancing the structural integrity of composite materials, and informing efficient drilling techniques.

As seen from the literature, although studies have been reported on UAD of different materials, the cutting parameters used were in the lower range of spindle speed and feed rate. In addition, only one study is available in the open literature on the UAD of GLARE using a low range of feed rates of up to 200 mm/min and spindle speeds of up to 2500 rpm [37]. The objective of this study is to address this research gap by evaluating the efficacy of the UAD system at spindle speeds of up to 7500 rpm and feed rates up to 750 mm/min, similar to those used in the CD and UAD of GLARE in previous studies. The current study expands on the previous one by investigating additional hole quality metrics, such as burr formation and hole size, which are more sensitive to higher cutting parameters. The work also shows the methodology for modelling the CD and UAD processes using numerical approaches. A comparison was made to validate the adequacy of the simulation model with the results from the experiments.

2. Finite element modelling

Finite element simulation of the drilling process is needed to discover the drilling mechanics in depth. To predict the chip formation, cutting force variation, delamination at the interfaces between layers, and defects at the hole entrance and exit, a *meso*-model is built up.

2.1. Modelling of GLARE constituents

Since GLARE laminate comprises aluminium and glass fibre layers, a combination of material damage models for both layers is introduced into the *meso*-model. On this basis, a user-defined subroutine (VUMAT) is developed to model the dynamic failure of both layers under high-strain-rate deformation, which occurs during the drilling process.

2.1.1. Modelling the dynamic failure in Al2024-T3 sheets

Given the large deformations of material taking place under the high strain rate and high temperature of drilling, the Johnson-Cook constitutive model with dynamic failure model was used for Al2024 sheets, as shown in Eq. (1) [38].

$$\overline{\sigma} = \left[A + B\left(\overline{\varepsilon}^{pl}\right)^n\right]\left[1 + C\ln\left(\frac{\dot{\overline{\varepsilon}}^{pl}}{\dot{\varepsilon}_0}\right)\right]\left(1 - \left(\frac{T - T_{tr}}{T_m - T_{tr}}\right)^m\right) \quad (1)$$

In the context of the Johnson-Cook ductile damage criteria applied to Al2024 sheets, the plastic strain $\overline{\varepsilon}^{pl}$, reference strain rate $\dot{\varepsilon}_0$, and equivalent plastic strain rate $\dot{\overline{\varepsilon}}^{pl}$ are interrelated according to the following equation:

$$\overline{\varepsilon}_D^{PL} = \left[d_1 + d_2 exp(-d_3\eta)\right] \times \left[1 + d_4 ln\left(\frac{\dot{\overline{\varepsilon}}^{pL}}{\dot{\varepsilon}_0}\right)\right]\left(1 + \left(\frac{T - T_r}{T_m - T_r}\right)^m\right) \quad (2)$$

In this equation, A, B, C, n, and m are constants. The exponent m relates to the thermal-softening coefficient, while the exponent n corresponds to the strain work hardening coefficient. T, T_{tr} and T_m denote the current temperature, room temperature, and melting temperature of the material, respectively. The equivalent plastic strain at the onset of damage, ε_D^{pL} can be calculated using Eq. (2), which considers the material's plastic strain, strain rate, temperature, and specified constants. This equation allows for the determination of the critical plastic strain that initiates damage in Al2024 sheets according to the Johnson-Cook ductile damage criteria.

Where $\bar{\varepsilon}^{pl}$ is the plastic strain, $\dot{\bar{\varepsilon}}^{pl}$ and $\dot{\varepsilon}_0$ are equivalent plastic strain rate and the reference strain rate; A, B, C, n, m are constants; m and n are the power exponents of the thermal-softening and strain work hardening coefficients, respectively; d_1 to d_5 represents the failure parameters whereas, η represents the stress triaxiality. The mechanical and damage material properties of Al2024 used in the simulation are given in Table 1.

Following damage initiation, the material stiffness undergoes degradation. The behaviour that occurs after damage initiation, referred to as post-damage-initiation behaviour, is described by the damage evolution equation presented in Eq. (3) [40]. This equation incorporates the characteristic length L of the element, which helps reduce the mesh sensitivity to damage after its initiation. The damage variable evolves linearly with the relative plastic displacement $\dot{d}$, assuming a linear relationship between the damage variable and a significant amount of plastic displacement.

$$\dot{d} = \frac{L\dot{\bar{\varepsilon}}^{pl}}{\bar{u}_f^{pl}} = \frac{\dot{\bar{u}}^{pl}}{\bar{u}_f^{pl}} \tag{3}$$

The effective plastic displacement at failure, denoted as $\bar{u}_f^{pl}$, and the effective plastic displacement rate, represented by $\dot{\bar{u}}^{pl}$, are crucial parameters in failure analysis. These parameters provide valuable insights into the material's behaviour during the failure process. When the material stiffness is fully degraded, the meshed element is deleted based on Eq. (4) to avoid interpolation-based errors. Isotropic damage parameter D is used to find the reduced stiffness (E_d) of degraded material such that $0 < D < 1$; $D = 1$ is fully degraded material whereas $D = 0$ condition refers to perfectly intact material. Meshed elements are deleted from the simulation when $D = 1$. If the maximum damage condition $D_{max} = 0.99$ was used for deformed elements in Al2024, which guarantees that the elements will stay active in the simulation with a residual stiffness of at least 1 % of the original stiffness.

$$E_d = (1 - D) \cdot E \tag{4}$$

2.1.2. Modelling the dynamic failure in glass fibre layers

The progressive damage and failure of composites can be effectively modelled using the built-in 2D Hashin damage model in Abaqus/Explicit. However, it should be noted that this model is only compatible with elements formulated under the plane stress assumption [41]. To address the limitation and enable the modelling of composites with 3D stress states, a user-defined material subroutine (VUMAT) was developed. The VUMAT subroutine extends the capabilities of the built-in composite damage model to incorporate glass-fibre layers in GLARE. Utilizing the VUMAT subroutine requires the definition of 19 material constants to accurately account for damage propagation throughout the thickness of the composite. Originally, the VUMAT subroutine was designed to replicate damage caused by a projectile impact on a unidirectional carbon-fibre-reinforced plate [41]. In this implementation, the VUMAT subroutine considers the influence of orthotropic elasticity on the elastic stress–strain relationship, while assuming linear elastic behaviour for the undamaged material, similar to that observed in Al2024-T3. The undamaged Young's moduli and Poisson's ratios are employed to search and estimate the primary elastic constants within the VUMAT subroutine. It should be noted that damage initiation can occur at any of the glass fibre layers in the laminate. As damage initiates, the stiffness of the material gradually degrades, reflecting the evolving state of damage within the composite structure. To predict the damage in the matrix layer due to compression and tension Puck failure criterion was used because the Puck criterion gives much better results for matrix layer failure due to transverse compressive bending [41]. For the fibre layer, the Hashin failure criterion was used. The damage initiation criteria used for the glass fibre layers are given below:

Hashin's fibre tensile failure ($\sigma_{11} \geq 0$)

$$\left[\frac{\sigma_{11}}{X_{1t}}\right]^2 + \left[\frac{\sigma_{12}}{S_{12}}\right]^2 + \left[\frac{\sigma_{13}}{S_{13}}\right]^2 = 1; D_{ft} = 1 \tag{5}$$

Hashin's fibre compression failure ($\sigma_{11} < 0$)

$$\frac{|\sigma_{11}|}{X_{1c}} = 1; \ D_{fc} = 1 \tag{6}$$

Puck's matrix tension and compression failure

$$\left[\frac{\sigma_{11}}{2X_{1t}}\right]^2 + \frac{\sigma_{22}^2}{|X_{2t}.X_{2c}|} + \left[\frac{\sigma_{12}}{S_{12}}\right]^2 + \sigma_{13}\left[\frac{1}{X_{2t}} + \frac{1}{X_{2c}}\right]^2 = 1 \tag{7}$$

$$\sigma_{22} + \sigma_{33} > 0; D_{mt} = 1 \tag{8}$$

$$\sigma_{22} + \sigma_{33} < 0; D_{mc} = 1 \tag{9}$$

Where σ_{11}, σ_{22}, σ_{12} and σ_{13} are the stresses in different directions. X_{1t} and X_{2t} are the tensile strengths, while X_{1c} and X_{2c} compression strengths in both longitudinal and transverse directions with respect to the fibres. S_{12} and S_{13} are the shear strengths. D_{ft} and D_{fc} are the damage parameters for fibres while D_{mt} and D_{mc} are those for the matrix as shown in Eqs. (10) and (11).

$$D_f = 1 - (1 - D_{ft})(1 - D_{fc}) \tag{10}$$

$$D_m = 1 - (1 - D_{mt})(1 - D_{mc}) \tag{11}$$

These damage parameters are used to identify the overall fibre and matrix damage parameters to calculate the damaged stiffness matrix. The elements are deleted from the mesh during simulation when reaches the maximum damage condition $D = D_{max} = 1$ for any of these four damage variables [31]. The material properties for the S2 glass fibre layers are given in Table 2.

2.2. Workpiece-tool setup

Several measures are taken to reduce the computation time and lower the computation cost. First, only the front part of the drill bit that participates in the cutting work and interacts with the hole wall is introduced in the model and set to a rigid body since the drill will not deform or degrade due to its higher stiffness. Second, no thermal effects are considered in the model because it is assumed the limited temperature rise has no great influence on the cutting mechanics. Third, a selective mass scaling factor is used while making sure that it will not affect the results by no more than 1 %. The displacement at failure is an

Table 1
Al2024-T3 Material Properties for FE Drilling Simulations [39].

Basic mechanical properties							
Density ρ (tonne/mm³)		Youngs Modulus (*MPa*)				Poisson's ratio	
2.78×10^{-9}		72,000				0.33	
Johnson-cook plasticity model parameters							
A (*MPa*)	B (*MPa*)	C	n	m	(s⁻¹)	T_m (°C)	T_r (°C)
369	684	0.0083	0.73	1.7	620	620	20
Johnson-cook failure model parameters							
d_1	d_2		d_3		d_4		d_5
0.112	0.123		1.5		0.007		0

Table 2
S2-FM94 Material Properties for FE Drilling Simulations [42 43].

Parameters	E_{11}	E_{22}	E_{33}	G_{12}	G_{23}	G_{13}	ν_{12}	ν_{23}	ν_{13}
Units	MPa	MPa	MPa	MPa	MPa	MPa			
Values	53,980	9412	9412	3000	5548	5548	0.33	0.0575	0.0575
Parameters	X_{1T}	X_{1C}	Y_{2T}	Y_{2C}	Y_{3T}	Y_{3C}	S_{12}	S_{23}	S_{13}
Units	MPa	MPa	MPa	MPa	MPa	MPa	MPa	MPa	MPa
Values	2430	2000	50	150	50	160	76	50	50

important influencing factor of simulation precision. Normally it is suitable to take a value from half to one element size. Besides, the displacement at failure is related to strain rate as well. As the strain rate increases, the strain at failure also increases [44]. These relations have been seen for different kinds of materials [45–47]. Stain rate depends both on the feed rate and the spindle speed such that it increases with the increase of both cutting parameters. In building up the simulation model for UAD of Glare laminates, there are some special considerations in the aspects of interaction and meshing.

2.3. Interaction

The contact algorithm employed in the analysis involves the utilization of a general contact formulation coupled with surface-to-surface interaction. This enables the characterization of interactions between the workpiece and the tool, as well as interactions within the workpiece itself. The algorithm accounts for element deletion that occurs after complete degradation. For the tool-workpiece interaction, two contact interaction properties are defined. Initially, the tangential behaviour is modelled using the penalty method. To represent the coefficient of friction within a reasonable range for various tool materials, a value of 0.7 is chosen, considering that values between 0.5 and 0.8 are commonly observed [48,49]. In addition, the normal behaviour is defined by utilizing the hard contact pressure over closure approach. Tie constraints are established to connect the aluminium sheets with the fibre layers, employing the surface-to-surface discretization method. This approach ensures the accurate representation of the interactions between the various components, allowing for a comprehensive analysis of the drilling process.

2.4. Meshing of the drill and workpiece

To ensure the accurate prediction of the thrust force during the drilling process, careful consideration of the computational model's mesh size is essential. In this study, the workpiece consisting of aluminium sheets and glass fibre layers with dimensions of $8 \times 8 \times 5.96$ mm was meshed using appropriate elements. The aluminium sheets were meshed with 8-node linear brick elements (C3D8R), whereas the drill bit was meshed using 10-node modified quadratic tetrahedron elements (C3D10M). To determine the optimal mesh size, a mesh convergence study was conducted, aiming to balance between computational accuracy and cost as shown in Fig. 1.

The study aimed to identify the mesh size at which further refinement would yield negligible improvements in cutting force prediction accuracy. Based on the mesh convergence study, specific mesh sizes were selected for the aluminium sheets and the glass fibre layers with a total number of 109,590 elements for the workpiece. Increasing the number of elements to around 120,000 doubled the computational time with less than a 2 % change in result. Therefore, a mesh size of 0.15 mm and 0.133 mm was employed in the stacking direction and 0.2 mm in the rolling direction around the hole as illustrated in Fig. 2. Additionally, larger elements were used to mesh the outer area surrounding the hole. The drill was only allowed to move in the Z-axis (feed rate) and rotate freely in the X-Y plane (rotational speed) both of which were applied to the reference point on the drill. The workpiece was fully constrained on
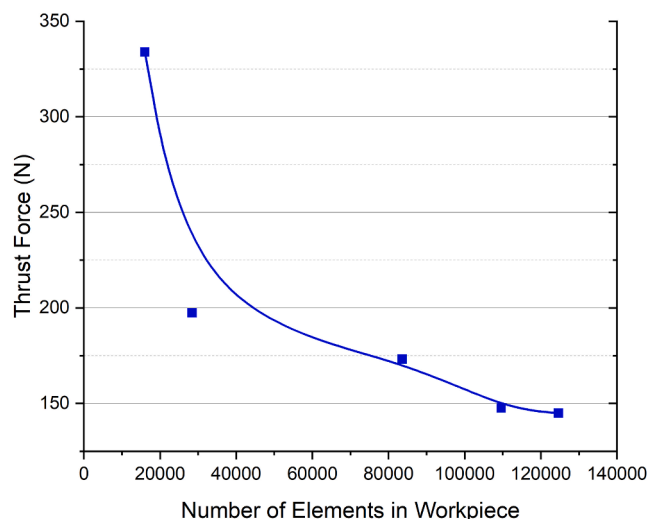
Fig. 1. Mesh convergence study for the drilling of GLARE laminate.

its four sides (Encastre U1 = U2 = U3 = UR1 = UR2 = UR3 = 0) as shown in Fig. 1. For UAD tests, the ultrasonic vibration frequency and amplitude were applied to the drill to simulate the vibratory motion during the drilling process and the feed rate was imposed on the workpiece.

3. Materials and methods

The drilling experiments were conducted utilizing an Ultrasonic-850 machine tool with a maximum spindle speed of 10,000 RPM and a power of 5.5 kW as shown in Fig. 3. Drilling experiments were carried out on GLARE 2B 11/10–0.3 laminate using 4 mm solid carbide twist drills coated with AlCrN. The twist drill designation is D4*24*SD4*50 and comprises two flutes, characterized by a point angle of 140°, a helix angle of 30°, a rake angle of °16, a lip relief angle of 14°, a chisel edge length of 0.3 mm and a chisel angle of 48°. The drills were supplied by Xiamen Jinlu Cemented Carbide Co Ltd in China.

The experimental design encompasses four distinct levels of feed rates and spindle speeds, both in the presence and absence of vibration. During Ultrasonic Assisted Drilling (UAD) trials, we utilized a vibration frequency of 18.7 kHz, matching the natural frequency of the ultrasonic tool holder associated with its longitudinal vibration mode. We applied an amplitude of 16 μm, corresponding to the maximum vibration amplitude observed in the ultrasonic tool holder when using a 4 mm twist drill. Notably, given the inverse relationship between thrust force and vibration amplitude, this parameter adjustment holds the potential to concurrently mitigate surface roughness and transverse deflections within the workpiece. [25,50]. In addition, drilling at frequencies close to 20 kHz was reported to reduce the maximum chip length [24]. Three drilling runs were carried out in total (96 holes) to confirm the repeatability. The details of the experimentation are given in Table 3. The mechanical properties of materials for the workpiece are shown in Table 4.
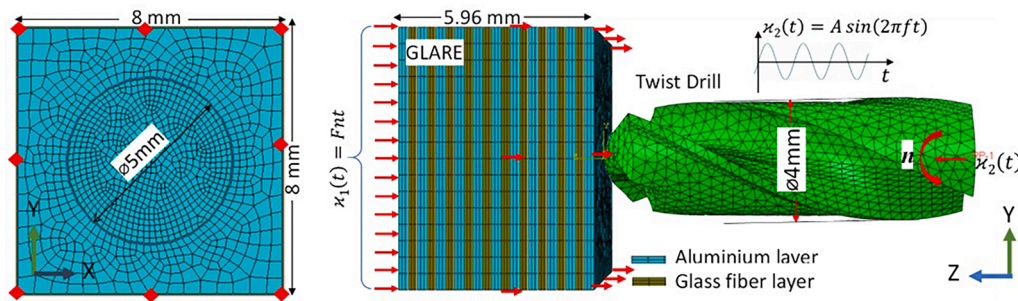
Fig. 2. Workpiece-Drill setup for drilling simulation.

Fig. 3. Schematic presentation of Machine setup for drilling tests [37].

Table 3
Details of the experimental plan for the drilling tests.

Parameters	Level 1	Level 2	Level 3	Level 4
Feed rate (mm/min)	300	450	600	750
Spindle speed (rpm)	3000	4500	6000	7500
Cutting speed (m/min)	37.7	56.55	75.40	94.25
Vibration-Amplitude (μm)	0 μm (for all CD tests)		16 μm (peak to peak for all UAD tests)	
Frequency	18.7 kHz (only used for UAD tests)			

Table 4
Mechanical properties of GLARE laminate constituents [51,52].

Material type	Properties	Values	Units
Al2024	Density	2770	kg/m^3
	Thermal expansion coefficient	23.4	(1/$^\circ$C) 10^{-6}
	Thermal conductivity	121	W/m-k
S2 Glass fibre	Density	1980	kg/m^3
	Thermal expansion coefficient	3.9–6.1 26.2–55.2	(1/$^\circ$C) 10^{-6}
	Thermal conductivity	1.1–1.4 0.43–0.53	W/m-k
Epoxy resin	Density	1130	kg/m^3
	Young Modulus	84	GPa
	Ultimate tensile strength	4400	MPa
GLARE 2B 11/ 10–0.3	Metal Volume Fraction	55.3 %	——

3.1. Thrust force measurement and setup

A KISTLER 9119AA dynamometer attached to a data acquisition system type 5697A1 and an 8-channel charge amplifier type 5080A was used to measure thrust force. Dynoware software version 3.2.5.0 was used to process and plot the date of the thrust force with respect to time. Eq.12 was used to calculate the percentage reduction in thrust force (PRTF) for UAD relative to CD.

Percentage reduction in thrust force (PRTF)

$$= \frac{\text{Thrust force CD} - \text{Thrust force UAD}}{\text{Thrust force CD}} * 100\% \qquad (12)$$

3.2. Surface roughness metrics measurement

This study introduces both 2D and 3D roughness metrics that contribute to a comprehensive evaluation of surface characteristics. Specifically, the average line roughness parameters R_a and R_z, along

with individual aerial roughness parameters S_a and S_z for both aluminium sheets and glass fibre layers, are examined. These metrics play a crucial role in establishing criteria for component acceptance or rejection. To assess the roughness of the drilled holes, a dual-instrument approach was adopted. Firstly, the 2D surface roughness metrics (R_a and R_z) were determined through the utilization of the Mitutoyo SJ-210 employing the contact method as illustrated in Fig. 4a. This assessment method captured the average surface roughness across the metal sheets and glass fibre layers. The 2D roughness metrics were measured using a sampling length of ($\lambda_c = 0.8$ mm, PC75 filter, ISO 4287:1997) and a traversing length that covers the whole hole depth to account for all the metal sheets and glass fibre layers in the laminate. The roughness device was calibrated using a Mitutoyo Precision reference specimen before any measurements. The roughness measurements for each hole were taken at four points around its periphery from the hole entry to exit and the average of the four readings is reported in the results. Concurrently, the 3D aerial surface roughness (S_a: roughness average and SR_z: average max height) of the individual aluminium sheets and glass fibre layers was measured using the Zygo Zegage optical aerial profilometer according to ISO 25178–2 at the centre of the hole, as shown in Fig. 4b. ZeMaps and MetroPro surface analysis software facilitated the meticulous evaluation of scanned regions, thereby enabling the derivation of precise roughness metrics for both the metal sheets and glass fibre layers. In addition, 2D roughness R_a and R_z measurements were extracted from the aerial 3D images by constructing a line at its centre to mimic that obtained when using a 2D roughness profilometer

measurement. For geometrical measurements, the full details of the Coordinate measuring machine (CMM) measurement of the hole size at the entry and exit can be found in a previous study [53]. Finally, the quality of the hole surface was analysed using a scanning electron microscope (Hitachi SU5000). An optical microscope was used to observe and record the burr formation at both the entry and exit. ImageJ software was used to calculate the area of the burr around the hole. Two circles that contain the burr were drawn, and the area between them represented the burr size as illustrated in Fig. 4c.

4. Results and discussion

4.1. Thrust force (F_z) analysis

Fig. 5a shows the thrust force profile for the CD and UAD testing at n = 3000 rpm and f = 600 mm/min. From both curves, it was observed that the thrust force shows different values when in contact with GLARE constituents due to the difference in properties [13,54]. Higher thrust force was observed when the drill was engaged with the aluminium layers than the S2 glass fibre layers. These observations are well-known and were described in former studies on CD and UAD of GLARE laminates [13,37]. The PRTF was plotted in Fig. 5b, which also shows the thrust force's sensitivity to cutting parameters and the presence/absence of vibration. Keeping the feed rate constant while increasing the spindle speed resulted in smaller chip thickness and therefore lower thrust force recorded. When the opposite is applied; the thrust force increases due to
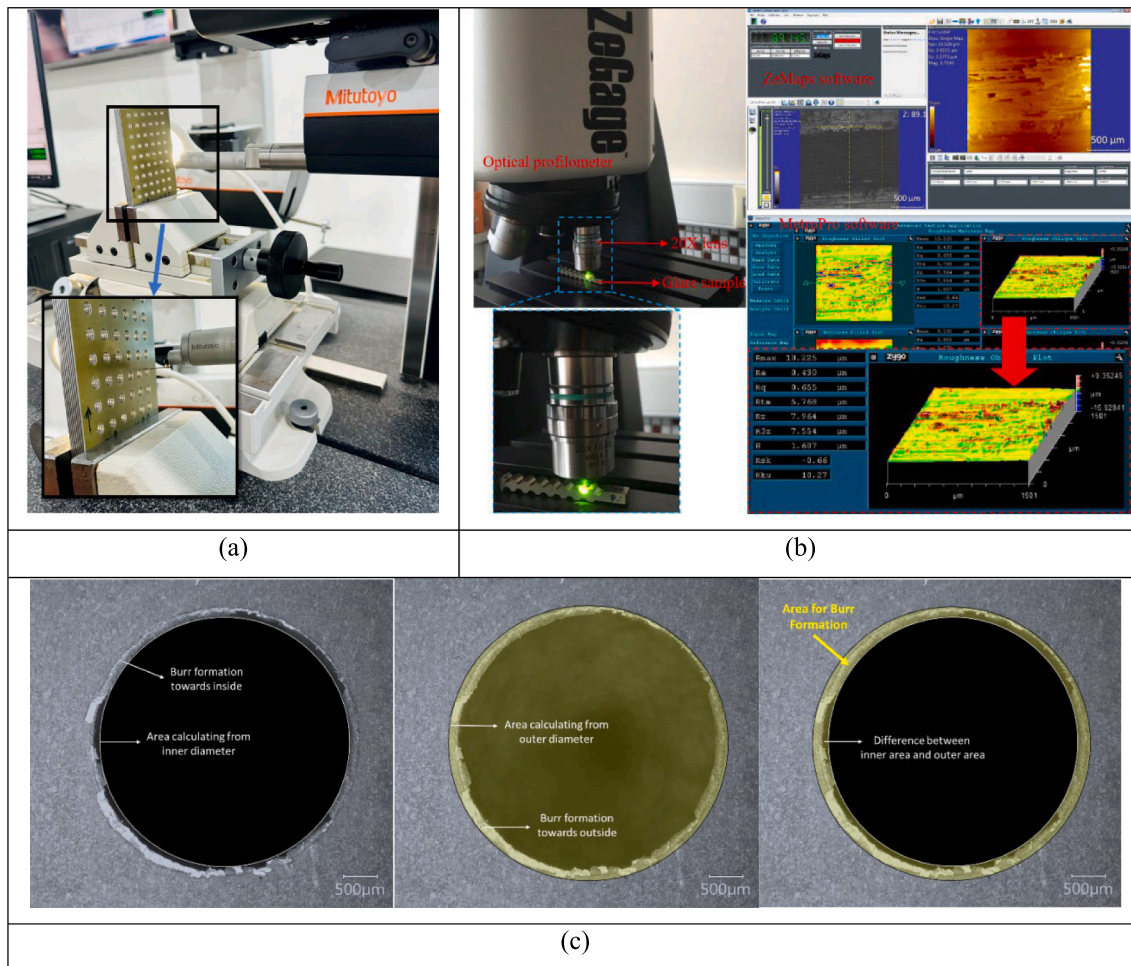

(a)   (b)

(c)

Fig. 4. Schematic illustration of the (a) 2D surface roughness tester (courtesy of Mitutoyo) (b) 3D surface roughness inspection (c) steps used to measure the burr area around the hole entry and exit, from left to right, 1st circle is placed at the hole edges, 2nd circle is placed to encompass the burr region, then the area is calculated via ImageJ area function.
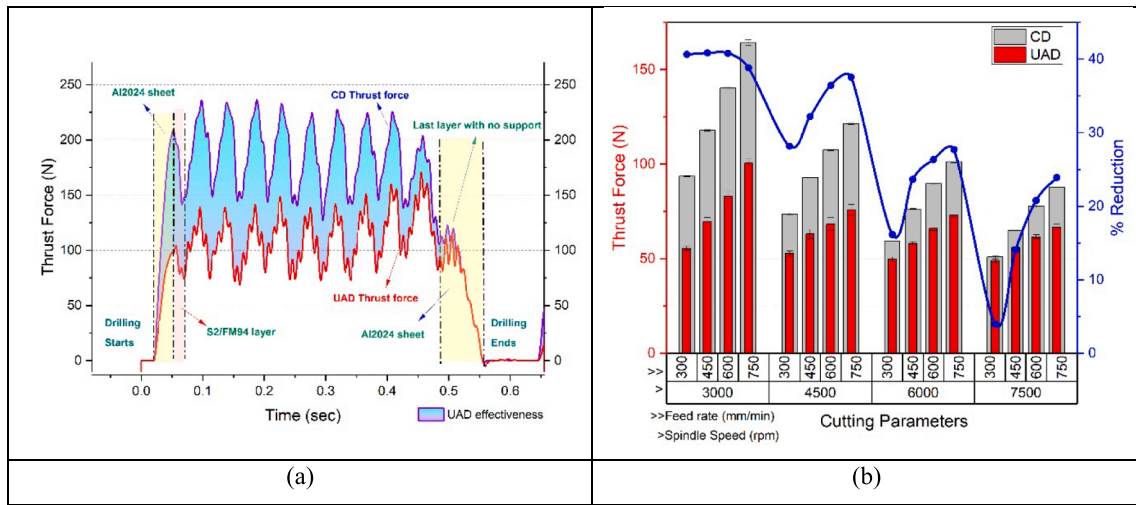
Fig. 5. Comparison of (a) thrust force for CD and UAD during 3000 rpm and 600 mm/min and (b) the effect of cutting parameters on thrust force in CD and UAD tests.

increased chip thickness. The trend observed here was also observed in a previous study when using a lower range of cutting parameters [37].

Fig. 5b shows the impact of cutting parameters on the efficiency of the ultrasonic system in decreasing the thrust force. While maintaining the constant feed rate and increasing the spindle speed, the PRTF decreases because of the reduced vibration frequency per unit of cutting length [55,56]. From this, it can be said that if the spindle speed were increased while the feed rate was held constant, the vibrational capability to dampen the thrust force would be reduced. The PRTF was also found dependent on the feed rate. Apart from drilling at 3000 rpm, the PRTF increased with the increasing feed rate consistent with the results reported from a previous study [37]. Notably, in the context of the lowest spindle speed and highest feed rate, the PRTF increased to a remarkable 64.84 %. As the uncut chip thickness increases, the negative thrust force caused by the chip resistance also increases when the drill moves opposite to the feed direction due to the sinusoidal movement of the drill. This trend was also observed in previous studies when drilling different materials [57,58]. On average, a PRTF of 28.24 % was observed during experiments by changing the drilling parameters in which the feed rate contributed somewhat equally to spindle speed. The lowest PRTF (3.97 %) was observed at the lowest feed rate and highest spindle speed, whereas the highest PRTF in thrust force (40.83 %) was seen at the lowest spindle speed regardless of the feed rate used.

Fig. 6 shows that for the holes machined using feed per rev of 0.1

mm/rev, the PRTF reduces with the increase in spindle speed. Consequently, elevating the spindle speed leads to a decreased frequency of vibrations per unit cutting length which diminishes the effectiveness of the ultrasonic system in reducing the thrust force. This observation underscores a vital connection: a higher frequency of vibrations per unit cutting length tends to enhance overall process effectiveness. As a result, we infer that increasing the vibration frequency during UAD substantially bolsters drilling process efficiency, directly yielding a noteworthy reduction in resultant thrust force. The thrust force also depends on the chip load, which is linked to both the spindle speed and feed rate. As the chip load increases, the thrust force increases for both CD and UAD, but the increase in thrust is smaller compared to CD with the increase in chip load.

According to Fig. 7, two observations can be made on how the UAD and cutting parameters influence the resulting thrust force. First, when comparing CD and UAD thrust force profiles, there is a noticeable variation observed in the first and last aluminium sheets. In CD tests, this is mainly due to the greater support available at the hole entry by the layers beneath. Meanwhile, at the exit, the lack of sufficient support from the following layers reduces the thrust force as there is less resistance to deformation and increased elastic deflection by the bottommost sheet and layer of the laminate. The opposite can be seen in UAD tests, the thrust force profiles in the last aluminium sheet are higher than that observed in the first one. According to Teimouri et al. [50], during
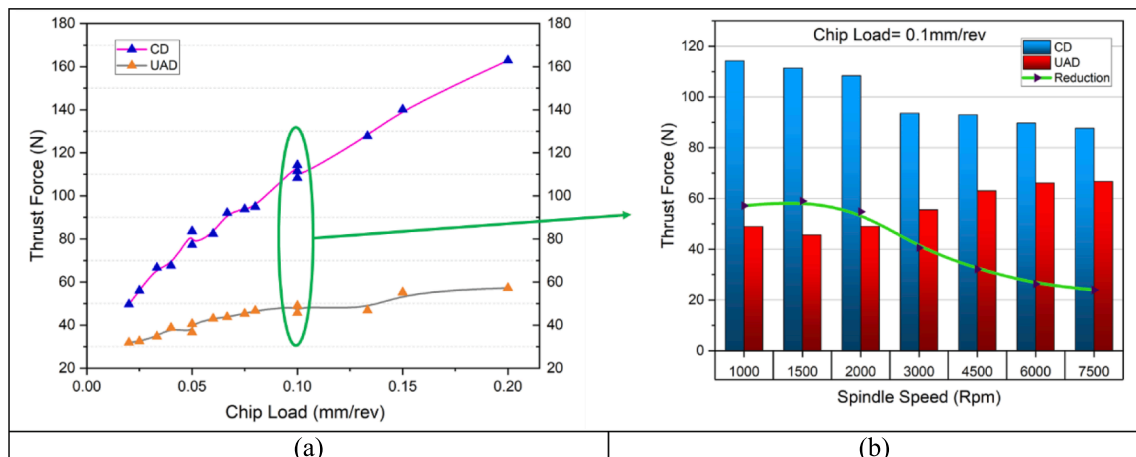

Fig. 6. Effect of (a) chip load and (b) spindle speed on the thrust force.
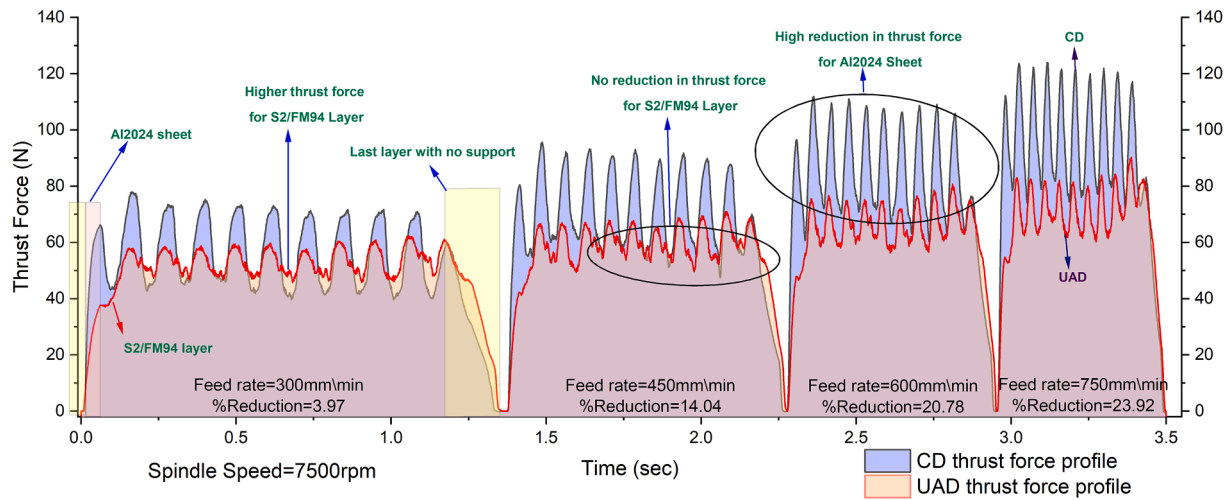
Fig. 7. Comparison of thrust force profiles for CD and UAD at 7500 rpm and different feed rates (each thrust profile is for a single hole, the total shown is the thrust force profile for four holes).

the UAD process, there are constant periodical engagements and disengagements between the tool and the workpiece in the thrust force–time diagram - such that the thrust force is zero when there is no engagement due to the constant vibratory motion of the drill. As shown in Fig. 7, when the feed rate increases, the effectiveness of UAD in reducing the thrust force also increases while drilling through glass fibre layers. For instance, the thrust force when the tool is removing the glass fibre layers under UAD is higher than that observed under CD at 7500 rpm and 300 mm/min. This means that at those cutting parameters, the effectiveness of UAD in reducing thrust force in the glass fibre layers is diminished. The effectiveness of UAD in reducing the thrust force in glass fibre layers increases when the feed rate increases. The same trend can be seen at 6000 rpm (see Appendix A). During CD and UAD comparison, the difference between each layer's thrust force profile peak increases when the feed rate increases. This leads to the conclusion that there is a proper combination of cutting parameters that would yield a maximum reduction in thrust force in both GLARE constituents rather than in one at the expense of the other. Indeed, Xiao [59] reported that the PRTF is maximum when using a spindle speed of 3500 rpm when drilling glass fibre composites. Their results indicated that by increasing the spindle speed beyond 3500 rpm while keeping the feed rate constant, the impact of ultrasonic vibration is diminished as a result of reduced tool-to-workpiece engagement.

Table 5 displays the influence of the drilling parameters on the drilling process as determined through analysis of variance (ANOVA).

The results show the percentage contribution of three factors in full factorial analysis from the current study as well as the ANOVA results from a previous study [37]. The highest contribution was due to the vibration with 31.14 % followed by a somewhat equal contribution by the spindle speed (28.11 %) and the feed rate (26.47 %), respectively. It can also be seen that for the current study -where higher cutting parameters are used- the percentage contribution of the vibration is less (31.14 % vs 58.27 % in the previous study) where a lower range of cutting parameters was used. This confirms the earlier finding, which indicates that the effectiveness of the ultrasonic system decreases with increasing the spindle speed. Therefore, to maintain the high effectiveness of the ultrasonic drilling process, other parameters which control the vibratory system such as the amplitude and frequency should be investigated/adapted with the increase of cutting parameters.

4.2. Hole size analysis

Fig. 8 illustrates the influence of the cutting parameters on hole size at both the entry (top) and exit (bottom) points. The findings show that, on average, hole sizes were larger regardless of the drilling process. In addition, at the top, the deviation was within 8 μm of the nominal hole diameter, and at the bottom, it was within 18.3 μm. The hole size at the top was always smaller than at the bottom which could be attributed to the increased deformations near the hole exit. Although a slightly larger hole size can be seen in most of the holes using UAD, however, it was insignificant and did not exceed a few microns in most cases. It was also observed that for both CD and UAD, the hole size at the top increased with the increase in feed rate. Table 5 also shows that the only two significant factors that affected the hole size at entry were the feed rate (13.93 %) and the spindle speed (10.09 %). At a lower feed rate the chip thickness and penetration rate decrease which allows a stable drilling process and results in a more accurate hole size [60]. Meanwhile, no trend can be seen for hole size at the bottom for CD and UAD. According to ANOVA results, only the feed rate has some minor effect on the hole size at the exit (8.77 %). From the previous literature, the influence of UAD on hole size in Composite-metal stacks is not clear. Some studies reported that the UAD produces holes that are smaller in size than those produced using CD [26], while other studies reported an opposite trend [61].

In summary, the deviation in hole size plays an important role in the structural integrity of machined aeronautical structures. It is well known that "ideally" the size variation of a hole relative to its nominal diameter should be minimum to avoid premature fatigue failure and obtain optimum rivet joint performance [62]. In addition, when riveting
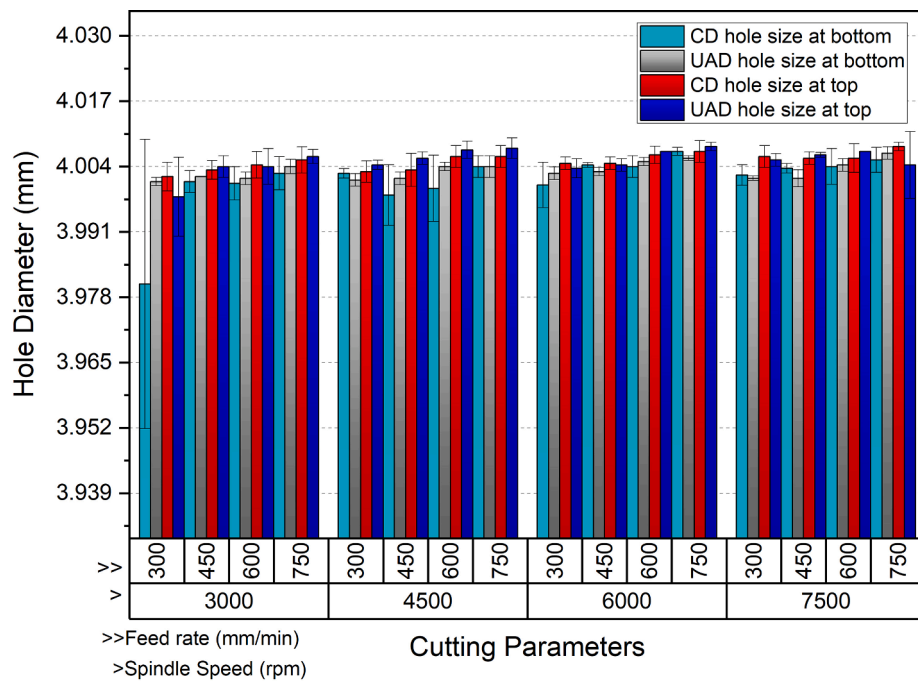
Table 5

Analysis of variance showing parameters with significant percentage contribution on thrust force and hole size at entry and exit.

Output	Thrust Force		Hole size	
Source	Current study	Previous study [37]	Entry	Exit
Spindle speed	28.11 %	11.34 %	10.09 %	NS
Feed rate	26.47 %	17.11 %	13.93 %	8.77 %
Vibration	31.14 %	58.27 %	NS	NS
2-Way Interactions				
Spindle speed*Feed rate	2.51 %	0.69 %	NS	NS
Vibration*Spindle speed	8.52 %	5.54 %	NS	NS
Vibration*Feed rate	2.76 %	5.69 %	NS	NS
3-Way Interactions				
Vibration*Spindle speed*Feed rate	0.11 %	0.37 %	NS	NS

*NS: Not significant (P-value is > 0.05).

Fig. 8. Hole size for CD and UAD tests under different drilling parameters at top and bottom.

aeronautical structures, the rivet's diameter should be slightly smaller than that of the hole it is being installed into. Ideally, a rivet should be placed in a hole which is a thousand of an inch larger in diameter (i.e., 101.6–152.4 μm). This is important since the process of deforming the tail (the end part of the rivet) into a head (also known as bucking) allows the rivet body to expand while inside the hole and securely hold the rivet in place. Therefore, the larger hole size is to ensure that the rivet can be easily inserted and then allowed to expand to tightly fill the gap and maximize strength. The deviation from nominal hole size ranged between -2 μm and $+8$ μm at the top, and between -19.3 μm and $+7$ μm at the bottom. These ranges are lower than those that were reported in earlier research on CD of GLARE laminates [11,12,63]. Of course, other factors might have contributed to the hole size in those previous studies which are not studied here such as the use of coolants, drill size, geometry, and coating. However, in comparison to other published research on CD of GLARE laminates and the suggested hole tolerance for aeronautical constructions, the variation in hole size shown in this study is within acceptable limits.

4.3. Surface roughness analysis

Fig. 9 shows the average surface roughness values in the laminate and its constituents for CD and UAD tests at different spindle speeds and feed rates. In Fig. 9a, 2D roughness values of R_a ranged between 1.29 and 1.71 μm and 1.35–1.75 μm for CD and UAD, respectively. In Fig. 9b, R_z ranged between 9.04 and 11.19 μm and 9.43–11.15 μm for CD and UAD, respectively. Generally, the average surface roughness results reported here are within the allowable range recommended in holes machined in aeronautical structures. R_a and R_z decreased for both CD and UAD when the feed rate was increased during constant-spindle-speed drilling. As the feed rate is increased, the cutting edge of the tool gets a proper cut which forms a uniform structure on the material surface, decreasing the surface roughness. In addition, low feed rates coupled with high spindle speeds cause the drill to rub around the hole rather than remove material from the hole. Excessive tool rubbing further elevates the temperature within the cutting zone. Consequently, ensuring optimal feed rates and spindle speeds becomes imperative, aimed at preventing undue rubbing. This strategy ensures that the

departing cut chip, in absorbing an adequate quantum of heat from the cutting zone, effectively mitigates its influence on surface roughness parameters R_a and R_z. It was also observed that drilling holes faster at 0.1 mm/rev reduced R_a and R_z. It has also been confirmed from the literature that UAD of composite materials (CFRP) and Composite/Metal stacks reduce the surface roughness by up to 50 % [21,26]. However, in the current study, UAD seems to have increased surface roughness in some instances by up to 11.3 % for R_a and 9.87 % for R_z. The increase in surface roughness metrics can be attributed to the ultrasonic vibration of the drill and the small thickness of the laminate constituents, which results in increased fuzziness of fibres during the cutting process caused by the continuous upward-downward motion of the tool. Previous research has shown that a decrease in thrust force is responsible for the improved surface finish achieved with UAD. [21,64], however, for the current experiments the same correlation is invalid.

Fig. 10(c, d), shows 2D surface roughness metrics (R_a and R_z) results for GLARE constituents captured at the centre of the hole using the 3D optical profilometry. The results indicate that the surface roughness in glass fibre layers is significantly higher than that in Al2024-T3 sheets. This in return indicates that the surface roughness in holes drilled in GLARE laminates is governed by the roughness of the machined glass fibre layers. These findings agree with previous studies reported on drilling GLARE laminates in the open literature [13,54]. Fig. 10 e and Fig. 10 f shows the aerial surface roughness measurements for the same hole at the same scanned region at the centre of the hole. Ther results show that the conclusion found earlier remains valid, however, it can be seen that the variation in roughness metric values for GLARE constituents are much less than those measured from a straight path (2D roughness) extracted from the 3D roughness profile.

It can be concluded that all the results of surface roughness show that using UAD does not yield any significant improvement in surface finish compared to CD. It is worth to mention that using 2D and 3D roughness measurement methods have their own advantages and limitations. Using 2D methods such as a stylus provides fast and easy measurement process. However, the measurement traces only one line on the surface which misestimate the real contact areas [65]. It is also limited by the size of the stylus tip limiting its ability to capture all valleys in the machined surfaces especially those that have high surface complexity
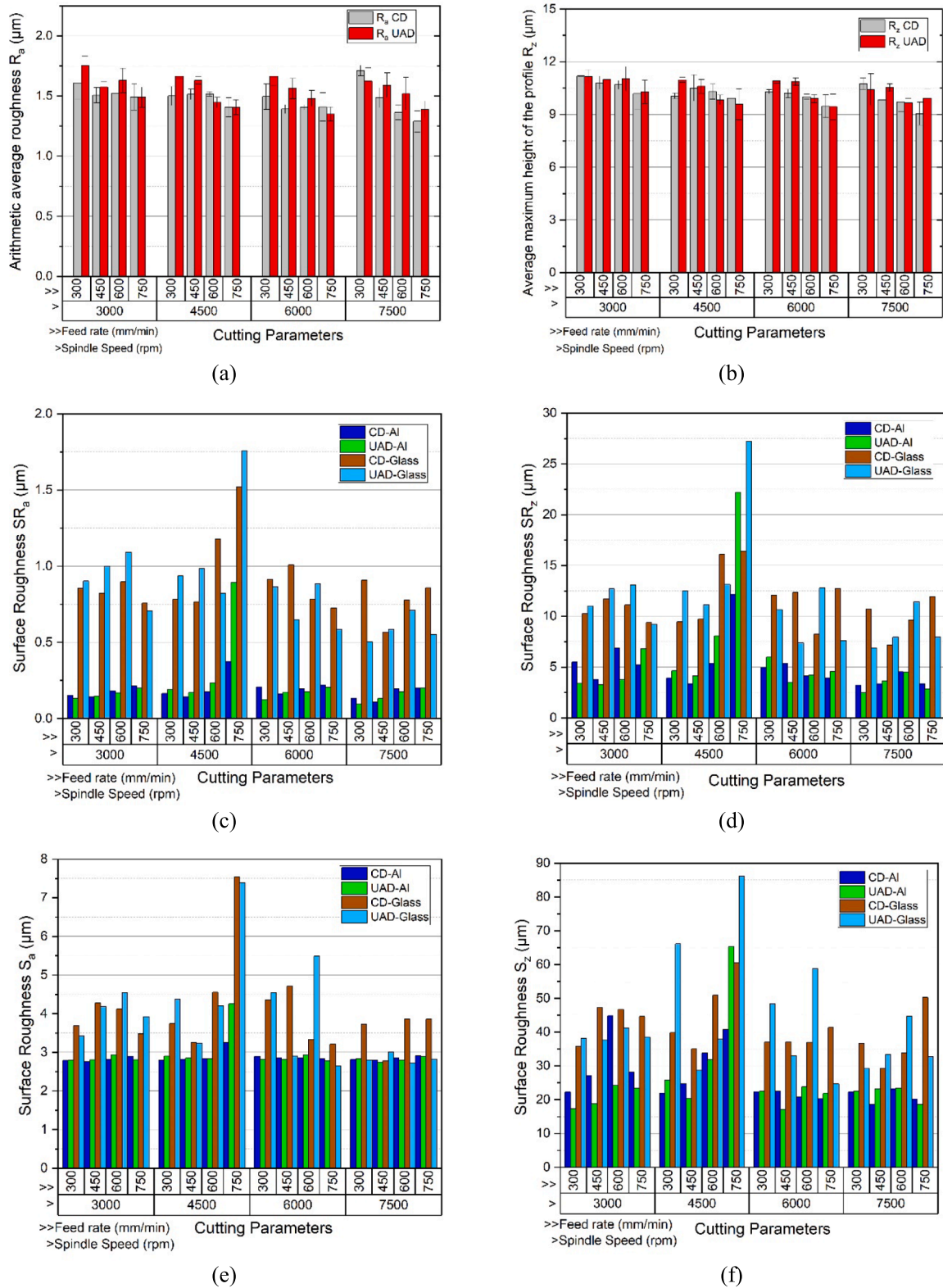
Fig. 9. Effect of drilling parameters on surface roughness metrics (a) R_a in GLARE using 2D profilometer (b) R_z using 2D profilometer (c) SR_a using 3D profilometer (d) SR_z using 3D profilometer (e) S_a using 3D profilometer (f) S_z using 3D profilometer.

such carbon/glass fibres. Similarly, 3D aerial roughness provides more robust surface evaluation method especially when the nature of the material requires using non-contact methods. However, 3D roughness methods can be time consuming to tolerate in a production environment and noise found in scanned sample can be an issue. Finally, a more realistic roughness evaluation using 2D profilometer would require conducting numerous measurements around the hole to increase the accuracy of the roughness values. Similarity, for 3D roughness measurements, larger aeras of the hole should be scanned and evaluated to fully capture the variations in surface finish throughout the whole hole.
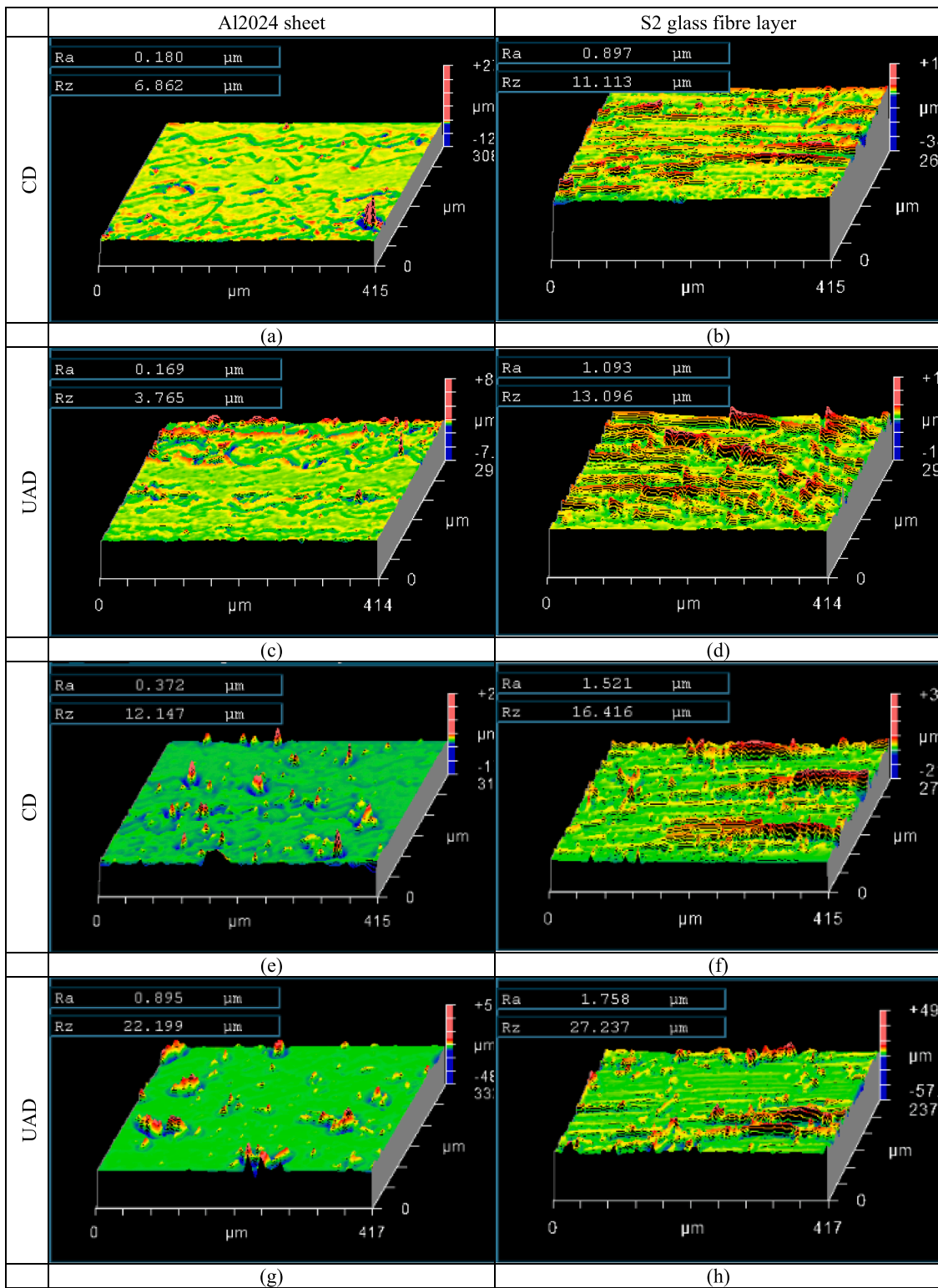
Fig. 10. Aerial surface roughness of holes drilled at (a-d) 3000 rpm and 600 mm/min (e-h) at 4500 rpm and 750 mm/min (i-l) at 7500 rpm and 300 mm/min for an aluminium sheet and S2 glass fibre layer (note: 2D roughness metrics were extracted from the aerial roughness map at a straight line from the centre of the hole).

The percentage contribution from the ANOVA results for surface roughness metrics is shown in Table 6 and compared with a previous study [37]. The feed rate appears to have the highest contribution on R_a followed equally by spindle speed and vibration. Meanwhile, for R_z, the trend is similar to that found previously showing that the vibration had no significant effect on the results. It can be also seen that the spindle speed effect becomes more significant at higher cutting parameters which indicates that when drilling holes at a faster rate, more attention should be given to the spindle speed and vibration amplitude.
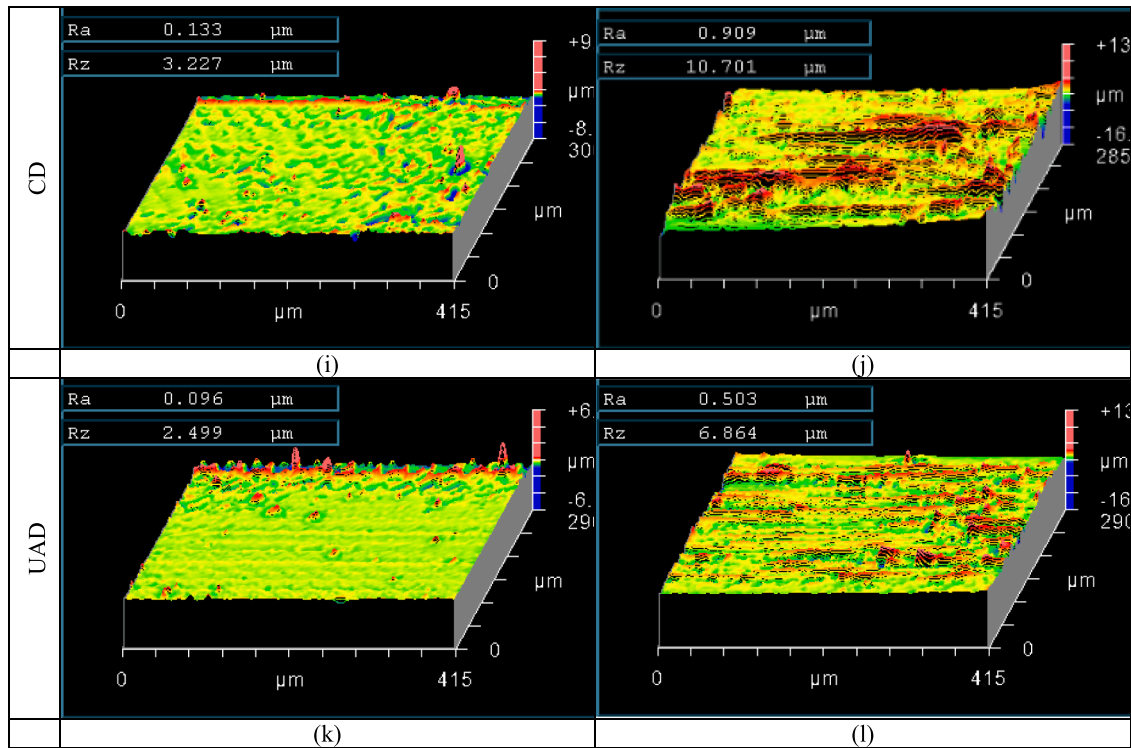
Fig. 10. (*continued*).

Table 6
Analysis of variance for drilling parameters with a significant contribution to surface roughness.

Source	R_a		R_z	
	Current study	Previous study [37]	Current study	Previous study [37]
Spindle speed	7.72 %	NS	17.20 %	6.79 %
Feed rate	36.10 %	NS	26.87 %	26.18 %
Vibration	7.12 %	NS	NS	NS
2-Way Interactions				
Spindle speed*Feed rate	NS	NS	NS	NS
Vibration*Spindle speed	NS	NS	NS	NS
Vibration*Feed rate	NS	NS	NS	NS
3-Way Interactions				
Vibration*Spindle speed*Feed rate	NS	NS	NS	NS

*NS: Not significant (P-value is > 0.05).

4.4. Burr formation analysis

Fig. 11 shows the average burr area (burr size) and maximum burr width formed around holes at the entry and exit. The results show that the entry burr area is small compared to that formed at the exit which is a well-known fact when drilling metals. Furthermore, UAD tests showed a significant reduction in the burr area around the hole exit. The thrust force directly impacts burr formation mechanisms in drilling, especially at the exit where the main failure mechanisms are due to bending and elongation [66]. This, in return, could explain the smaller burr size at the exit in holes drilled using UAD compared to CD at the same cutting parameters. For CD tests, increasing the feed rate resulted in a larger burr area at a constant spindle speed because of the higher thrust force, which causes more material deformation at the hole's exit and is aligned with the results reported for drilling Al2024-T3 and aluminium silicon carbide composites [38,67]. Similarly, Increasing the spindle speed

decreased the burr area at the exit in CD tests due to reduced uncut chip thickness and therefore reduced thrust force. Similar trends were reported in a previous study when drilling CFRP/Al stacks [68].

In general, the entry burr area for CD and UAD did not exceed 0.76 mm^2. Meanwhile, the exit burr area in under CD exceeded 3 mm^2 compared to around 0.56 mm^2 under UAD which highlights a distinct advantage for using UAD to create nearly burr free holes. This observation underscores a distinct advantage favouring the use of UAD in generating nearly burr-free holes. Particularly at a low spindle speed of 3000 rpm and a high feed rate of 750 mm/min, where the maximum reduction in thrust force was observed. there was a corresponding substantial decrease in exit burr area of up to 99 %. This reduction effectively eliminated almost all burrs at the exit and significantly diminished the entry burr area by 59 %. These same parameters also exhibited the most substantial reductions in burr width, with decreases of 94 % and 36 % at the exit and entry, respectively. The minimum exit burr area formation for CD was found at the lowest feed rate and highest spindle speed, whereas the maximum exit burr area was found at the highest feed rate and lowest spindle speed which matches the theory and causes behind the burr formation. Meanwhile, it was observed that the entry burr area in UAD was in some instances larger than that at the exit. Similarly, the maximum burr width at entry did not exceed 115 μm and 160 μm for CD and UAD, respectively. At exit, the maximum burr width reached slightly over ~200 μm and ~70 μm for CD and UAD, respectively. In UAD tests, the alternating motion of the drill due to the ultrasonic vibration helps the material to roll over and deform in the feed direction and therefore reduced burr size at the exit. Similarly, it was found that UAD reduced burr width at entry at 3000 and 4500 rpm, while the exit burr width was somewhat higher than in CD. For 6000 and 7500 rpm, there was no clear trend in burr width in holes from CD or UAD tests, but it was observed that UAD tended to increase the entry burr width. Fig. 12 below shows some images for hole entry and exit burrs from CD and UAD tests. As evident from the hole images below and the results in Fig. 11. The entry burr under UAD was greater than that at the exit at 6000 rpm and 7500 rpm.
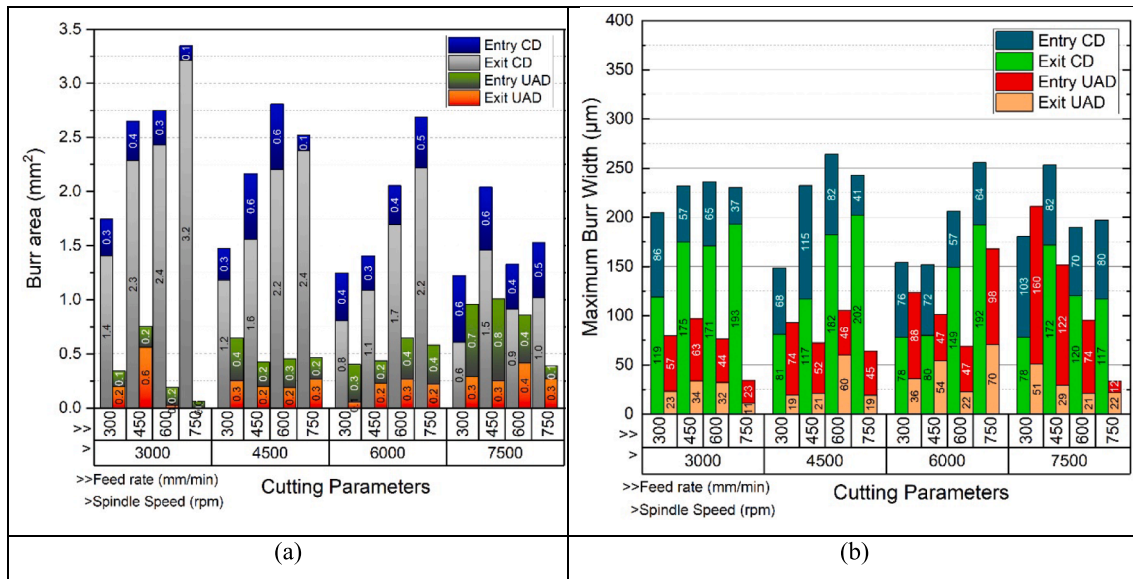
Fig. 11. Burr formation showing (a) burr area comparison (b) maximum burr width for CD and UAD tests at different drilling parameters.

4.5. Microstructural analysis using SEM

Matrix and chip debris, broken and bent fibres, fibre impressions, metal plastic flow, viscous flow, repeated stacking, and rollover burrs were found in both CD and UAD tests as shown in Fig. 13. An increase in feed rate resulted in greater fibre bending and debris. Under the same cutting parameters, the presence of fibre debris was greater in holes machined under UAD than CD which could indicate higher fragmentations and breakability of metal chips, matrix, and fibres due to the ultrasonic vibration as shown in Fig. 13b. This in return could also explain the slightly higher surface roughness found in holes machined using UAD. Similarly, segments of a broken matrix appear to adhere and cover the glass fibre layers and exposed cut fibres as shown in Fig. 13c. Fibre impressions were seen on the aluminium sheets in both CD and UAD tests which indicate that some broken fibres were unable to escape from the hole and rather adhered to the cutting tool then rubbed against the hole walls and sometimes forced in between the fibres as shown in Fig. 13d. Looking also at Fig. 13e and 13f, it can be seen that the surfaces of holes from CD tests were somewhat smoother and cleaner than those from UAD tests which could further explain the slightly higher surface roughness. Overall, SEM analysis showed that there is no noticeable difference in the hole quality for CD and UAD tests which could explain the negligible difference in surface roughness.

Fig. 14 presents SEM images captured under various cutting parameters for both conventional drilling (CD) and ultrasonic-assisted drilling (UAD). The quality of the machined holes, as revealed by SEM analysis, exhibits a notable sensitivity to feed rate and spindle speed. Specifically, we observed a significant influence on chip formation and adhesion to the machined surface. Under low spindle speeds and feed rates, CD produced discontinuous chips, which tended to adhere to the workpiece surface, resulting in suboptimal machining quality. In contrast, UAD generated smaller, serrated chips due to vibration assistance, facilitating easier chip evacuation at the entrance and consequently improving machining quality. However, at the hole exit, chip evacuation proved challenging, leading to surface scratches, as illustrated in Fig. 14 Notably, CD at low spindle speeds left distinct markings on the machined surface. These markings stem from chip separation through a deformation process, leaving visible imprints on the aluminium surface and diminishing machining quality. UAD, on the other hand, uses a vibrating drill to convert the deformation process into a cutting process while also imparting a polishing effect, ultimately enhancing machining quality. In contrast, the unique nature of glass

fibre exhibited minimal sensitivity to vibration, displaying little impact on machining quality, as it is less influenced by polishing and deformation processes.

At high-speed drilling, both CD and UAD exhibited effective chip evacuation, reducing the occurrence of welded chips on the machined surface. High cutting speeds primarily converted the deformation process into a cutting process, facilitating easy chip evacuation and thus improving machining quality while reducing deformation marks. Notably, there was a slight discrepancy between CD and UAD in machining the glass fibre layers at high cutting speeds. In summary, UAD proved less effective at high cutting speeds when assessing machining quality, with CD also capable of achieving high machining quality. The analysis of machined surface quality paralleled thrust force measurements when evaluating the effectiveness of UAD at different cutting speeds. The fibre-cutting process was notably influenced by fibre orientation, feed rate, and the type of drilling process employed. Smoother fibre layer cutting was observed when fibres were oriented at 90° to the cutting direction (as depicted in Fig. 14). However, when the angle between fibres and the cutting edge shifted to 45° degrees, uncut fibres and fibre breakage occurred, regardless of whether CD or UAD was utilized. The severity of uncut and broken fibres varied under different cutting parameters, with UAD showing more pronounced effects at low spindle speeds and feed rates due to ultrasonic vibration while CD exhibited these effects at low spindle speeds and medium feed rates. When fibre cutting occurred at 0°, various defects, such as fibre breakage, debonding, bending, and adhesion, were observed for both CD and UAD, as detailed in Fig. 14. Fibre breakage was more prevalent at high spindle speeds and low feed rates, while fibre adhesion was observed at the hole entry during UAD. Small broken fibres or bundles of broken/fibre matrix cannot be evacuated from the hole during drilling, which inadvertently become trapped between the tool body and the hole surface, causing them to be forced onto the borehole walls.

4.6. Comparison of thrust force: Experimental vs. Numerical results

Fig. 15a shows the comparison of thrust force profiles from the FE model and experimentation at 4000 rpm and 600 mm/min. The error in predicting the thrust force ranges from 1 % to 15 %. The large discrepancy in some of the results is due to the effects of strain rates in the metallic layers in the laminate. The relationship between the strain rate (which is affected by the cutting parameters) and displacement at failure was determined by performing simulation at (3000 rpm, 750
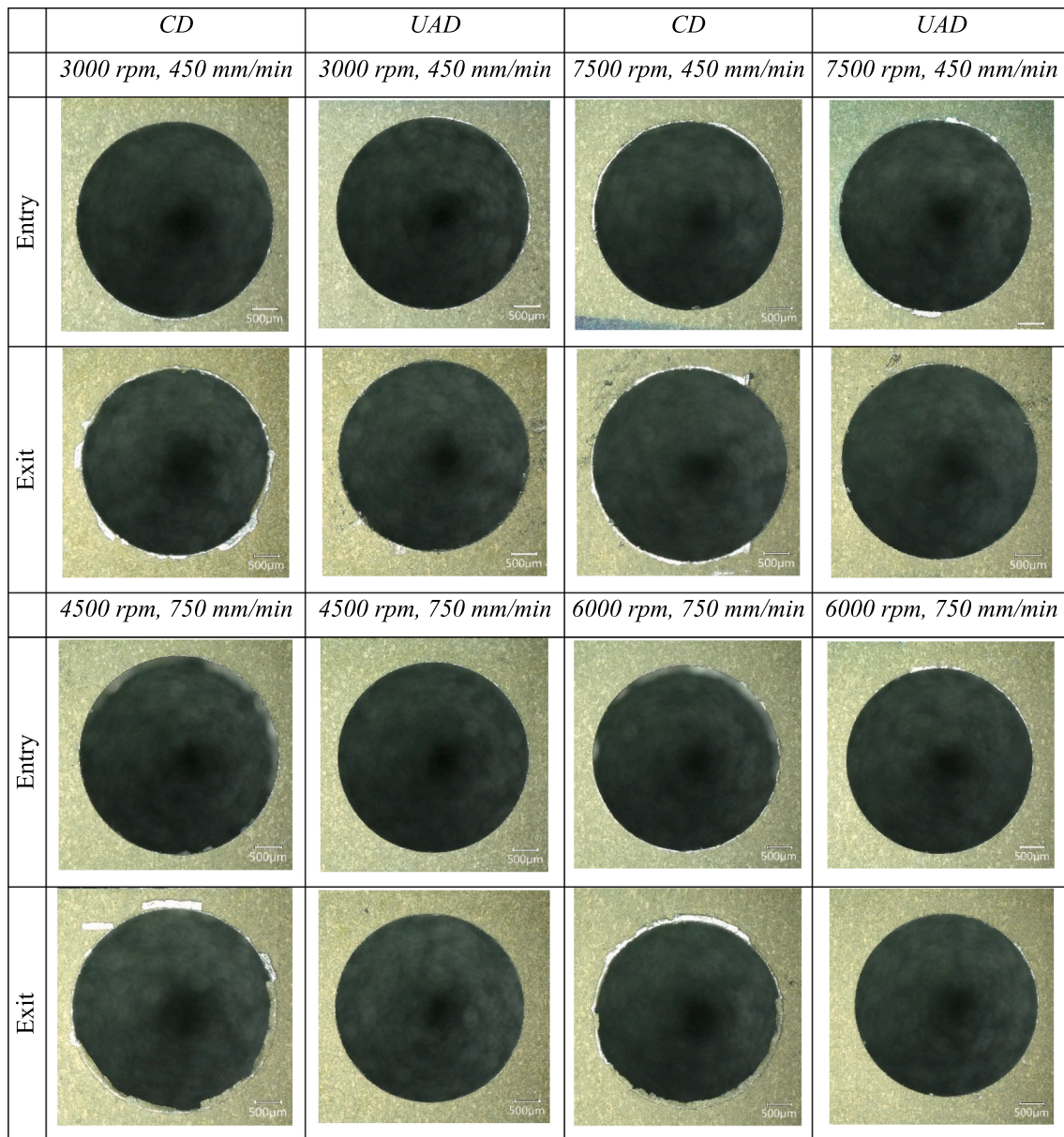
	CD	UAD	CD	UAD
	3000 rpm, 450 mm/min	3000 rpm, 450 mm/min	7500 rpm, 450 mm/min	7500 rpm, 450 mm/min
Entry				
Exit				
	4500 rpm, 750 mm/min	4500 rpm, 750 mm/min	6000 rpm, 750 mm/min	6000 rpm, 750 mm/min
Entry				
Exit				

Fig. 12. Hole images showing burr formation at entry and exit in holes from CD and UAD tests.

mm/min) and (7000 rpm, 750 mm/min). From these two simulations, a relationship was found between the strain rate and displacement at failure by using the interpolation method. The relationship between displacement at failure and chip load was used. Using this relationship and model, the error was reduced from (3.2 %–53.2 %) to (1 %–15 %) for the thrust force, which can be used to predict thrust forces more accurately.

The mesh size and scaling factor mainly affect the accuracy of the results. Smaller mesh size and scaling factor increases the accuracy but adds high computational cost; therefore, larger mesh size and mass scaling factor were used. Enhancing the accuracy of simulation results can be achieved by employing more realistic friction models that accurately represent the friction behaviour at the tool-workpiece and tool-chip interfaces [69]. A more realistic cutting tool model with deformable features can further enhance the results. The use of reduced integration elements leads to a degree of inaccuracy. Therefore, using full integration elements -although it will considerably increase the simulation time- can have a substantial impact on the quality of the integration utilized in stiffness matrix formulation and the element

deformation method. Fig. 14b shows the effect of cutting parameters on the resulting thrust force for the CD and UAD processes from the literature, current experimental results, and numerical simulation. The overall reduction in the thrust force was due to the impulse (cyclic) cutting of the tool, which reduces both cutting and contact time.

4.7. Stress and strain analysis

The progressive damage and the stress distributions in the laminate constituents (i.e., the metal sheets and unidirectional glass fibre layers) during the drilling process are shown in Fig. 16a. As can be seen from images (a) through (e), the stresses are induced in the laminate once the drill is in contact with the top surface. As the drill progresses into the workpiece, the metallic sheets undergo elastic than plastic deformations, while the glass fibre layers undergo orthotropic linear elastic behaviour depending on the fibre orientation [70]. Consequently, each of the laminate constituents fails according to the associated damage model (i.e., Johnson-Cook for the metal sheets and Hashin-Puck for glass fibre layers). When the elements meet the failure criteria, they
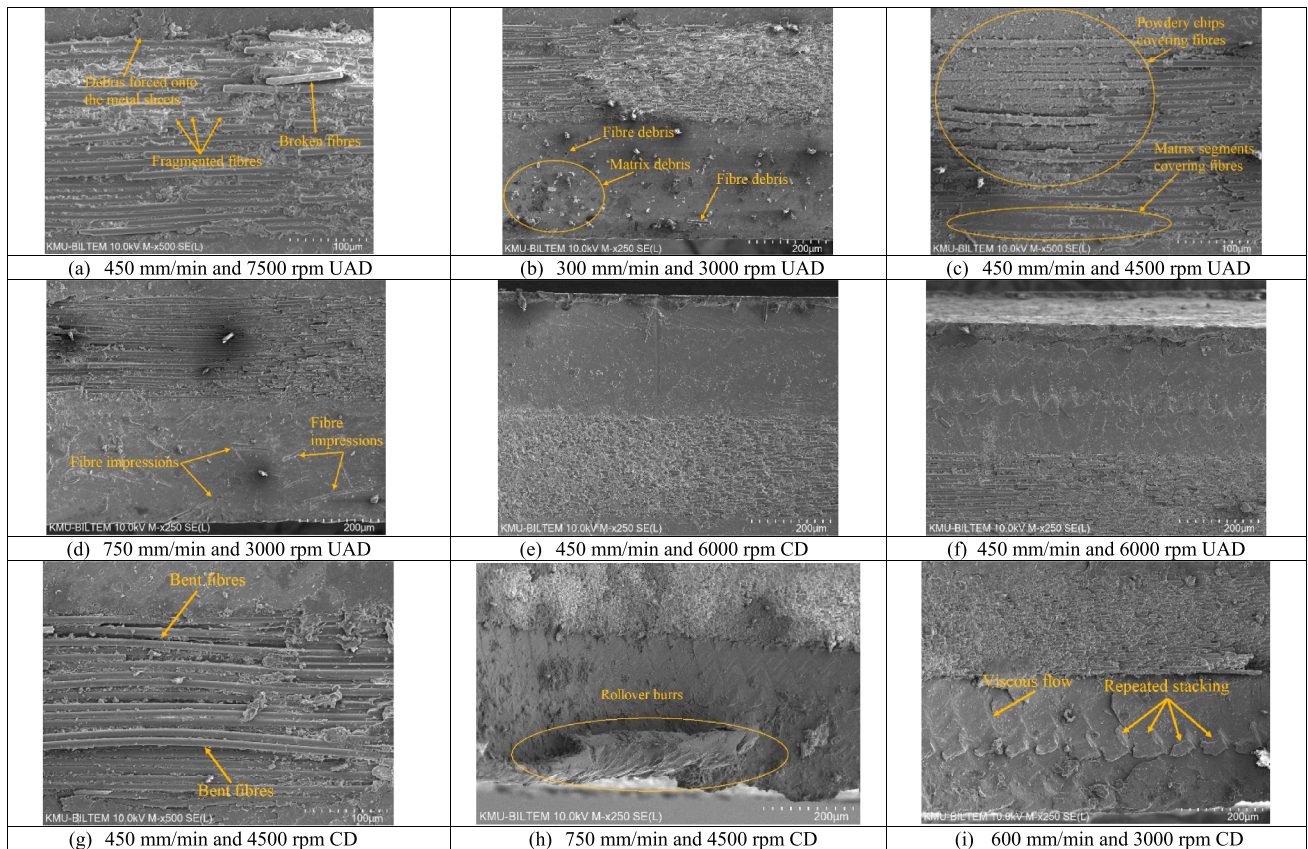
(a) 450 mm/min and 7500 rpm UAD	(b) 300 mm/min and 3000 rpm UAD	(c) 450 mm/min and 4500 rpm UAD
(d) 750 mm/min and 3000 rpm UAD	(e) 450 mm/min and 6000 rpm CD	(f) 450 mm/min and 6000 rpm UAD
(g) 450 mm/min and 4500 rpm CD	(h) 750 mm/min and 4500 rpm CD	(i) 600 mm/min and 3000 rpm CD

Fig. 13. SEM images of holes in UAD and CD tests.

3000 rpm, 750mm/min bottom UAD	4500 rpm, 750 mm/min bottom UAD	6000 rpm, 300mm/min bottom CD
4500 rpm, 450mm/min bottom CD		6000 rpm, 600mm/min top UAD
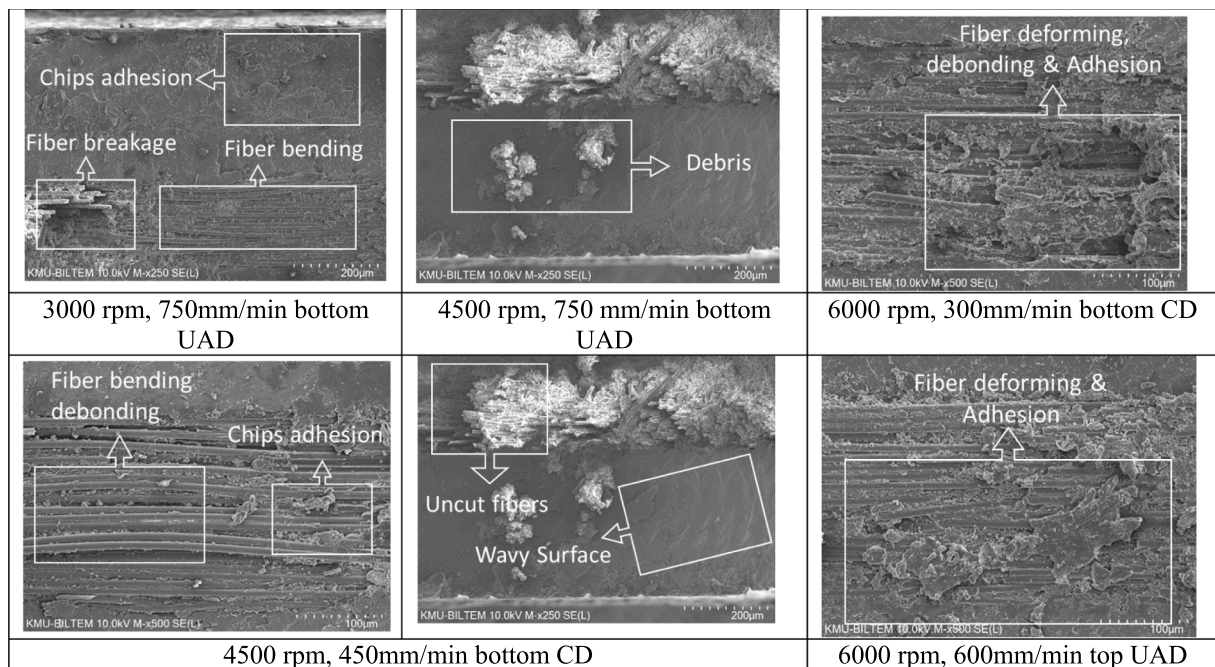
Fig. 14. SEM images of some of the defects observed at the top and bottom sections of drilled holes.

are removed from the model. From Fig. 16a comparison of conventional and ultrasonic-assisted drilling can be seen that the maximum stresses generated during CD are higher compared to UAD due to its lower thrust force. Higher deformation in the last layer of aluminium in CD increases the risk of causing delamination, whereas less deformation was caused at the last layer during the UAD process. The higher deformation also causes an increase in cutting time which can be seen in Fig. 15 from experimental data. Most of the CD processes have higher cutting time when compared with the same parameters of the UAD process. From Fig. 16a, it can also be seen that the UAD causes more stresses in the
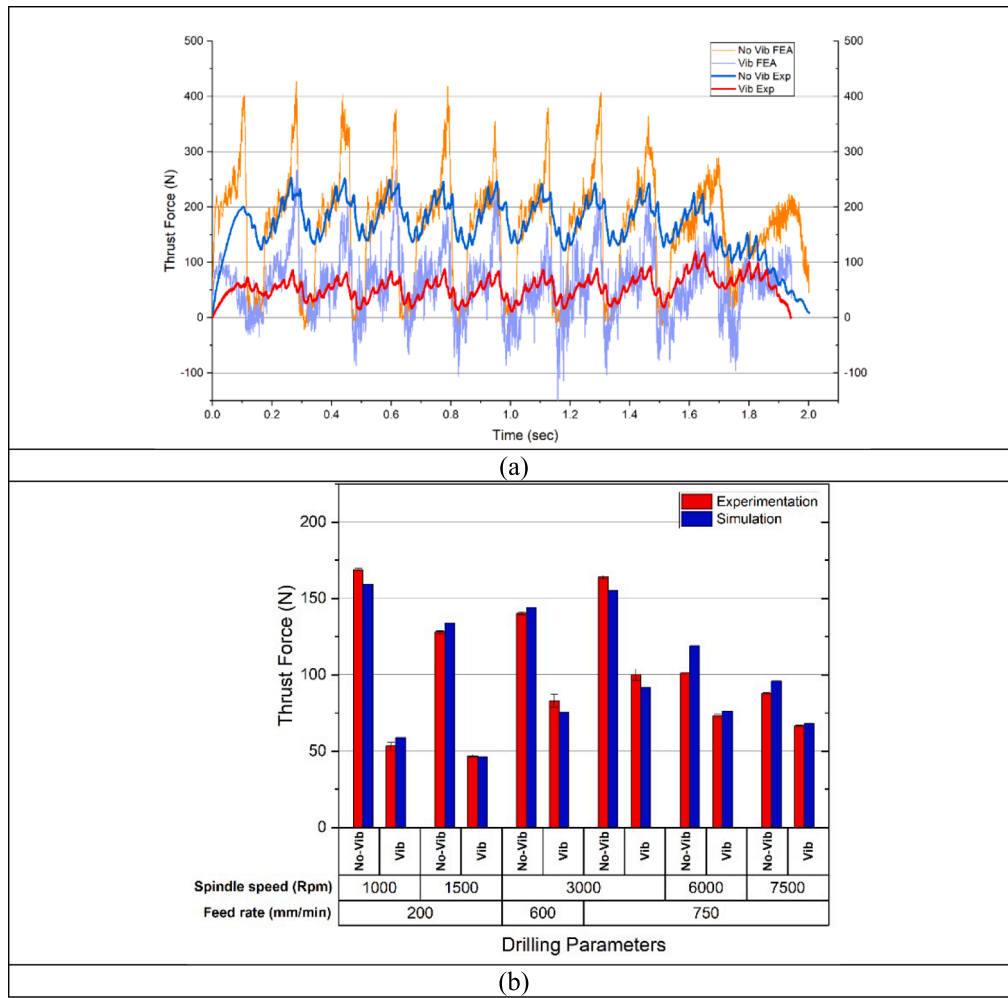
Fig. 15. Comparison of (a) thrust force for 1000 rpm and 200 mm/min and (b) Average thrust forces for different cutting conditions.

rotational direction, whereas CD causes more stresses and deformation in the feed direction. Smaller strain is distributed more widely during UAD due to cyclic force, whereas maximum strain can be seen during CD due to constant force, as shown in Fig. 16b.

5. Conclusions

This research investigates the effect of ultrasonic-assisted drilling of GLARE 2B fibre metal laminates under spindle speeds of 3000–7500 rpm and feed rates of 300–750 mm/min. This research aims to identify different aspects of UAD and CD of fibre metal laminate using a numerical modelling approach and how it is affected by different input parameters. It also investigates the influence that drilling parameters and vibration have on several hole quality metrics, including burr formation, hole size, surface roughness, and machined surface defects. The ultrasonic vibration was found to have the greatest impact on the thrust force during UAD tests (31.14 %), followed by the spindle speed (28.11 %) and feed rate (26.47 %), respectively. It was found that the most significant interaction was that between spindle speed and vibration. The main findings from the experimental and numerical analysis are summarised below:

1) The trends seen from the cutting parameters and vibration on thrust force in this study are similar to those reported in the previous study on GLARE laminates under a lower range of cutting parameters. However, it was found that the effectiveness of the UAD system was reduced by more than 27 % in comparison, which suggests that

drilling holes faster will diminish the ultrasonic system efficiency. A suggestion to overcome this reduction in efficiency could be adjusting the ultrasonic system parameters (i.e., vibration amplitude and frequency).

2) For both CD and UAD, the lowest thrust forces were recorded at a high spindle speed (7500 rpm) and a low feed rate (300 mm/min). The maximum thrust force reduction (40.83 %) was seen at a low spindle speed of 3000 rpm and for the feed rates of 300 to 600 mm/min. The observed trends here are in agreement with those seen in prior research on conventional and ultrasonic drilling of GLARE laminates.

3) Generally, holes were oversized in both CD and UAD. The hole size at the top was smaller than that at the bottom for CD and UAD tests. In addition, the results showed under the same cutting conditions, UAD tests produced holes that were slightly larger than CD tests. The feed rate and spindle speed were found to have some contribution to the hole size at the top, while only the feed rate influenced the hole size at the bottom.

4) The surface roughness in holes machined using UAD was slightly higher than their counterparts in CD. R_a ranged between 1.29 and 1.71 μm and 1.35–1.75 μm for CD and UAD, respectively. While R_z ranged between 9.04 and 11.19 μm and 9.43–11.15 μm for CD and UAD, respectively. The surface roughness in glass fibre layers was always higher than that in the aluminium sheets. Moreover, it was found that the surface roughness in glass fibre layers was reduced in UAD tests when drilling at higher spindle speeds of 6000 and 7500 rpm.
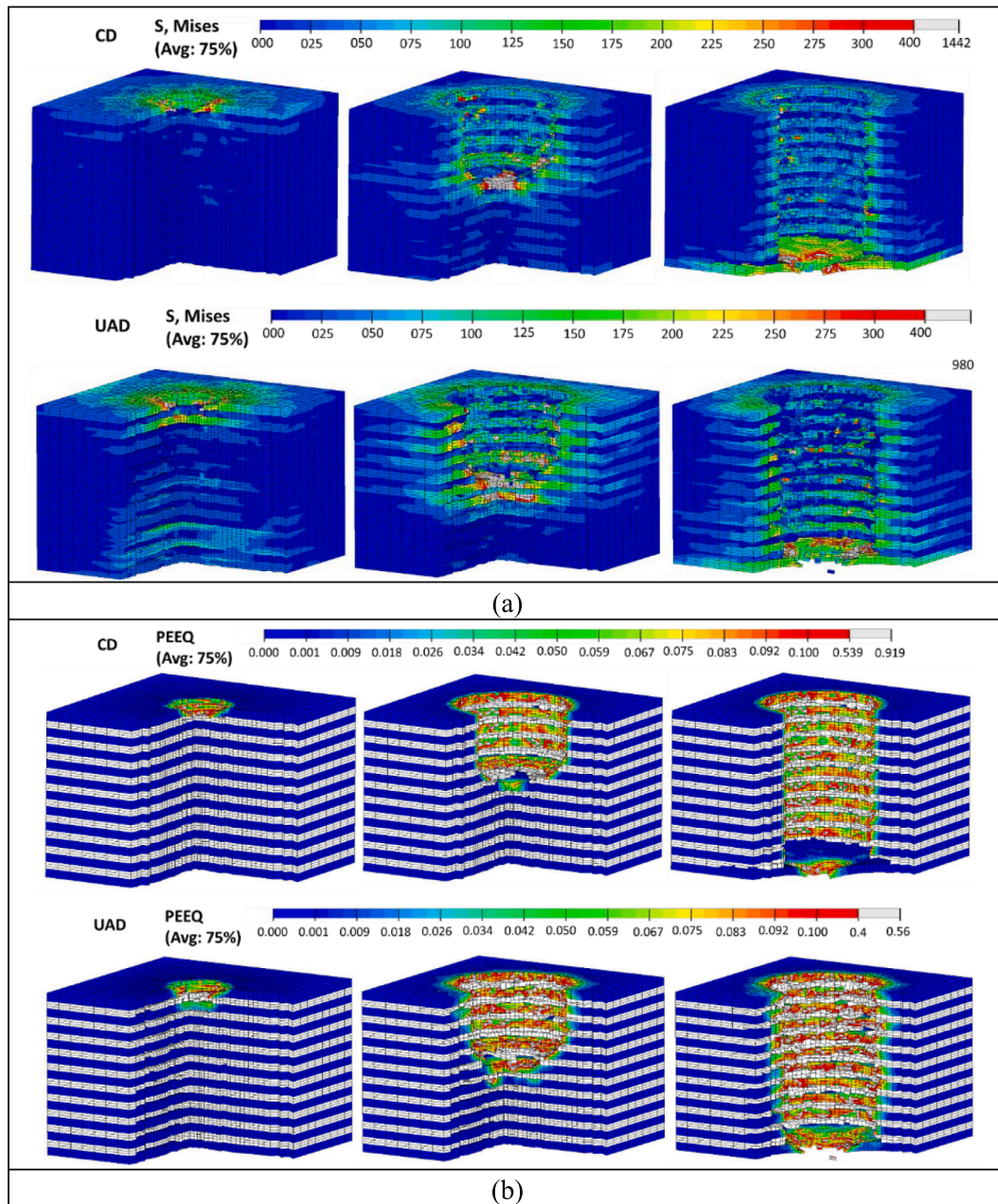
Fig. 16. FE results showing (a) S, Mises (Von Mises distribution) in the drilling process at 6000 rpm and 750 mm/min (b) PEEQ (Equivalent plastic strain) distribution in the drilling process at 6000 rpm and 750 mm/min.

5) R_a was mostly influenced by the feed rate (36.10 %), followed by the spindle speed (7.72 %), and the ultrasonic vibration (7.12 %). For R_z, only the feed rate (26.87 %) and the spindle speed (17.20 %) had an effect according to ANOVA.

6) The burr width and area formed at the hole's exit using CD was significantly larger than at its entry. In addition, the burr width and area at the exit under UAD was much smaller than in CD tests under the same cutting parameters. Furthermore, the exit burr width and area under UAD were occasionally smaller or equivalent to those at the entry especially at higher spindle speeds of 6000 and 7500 rpm. This indicates that using ultrasonic drilling can significantly reduce burrs at the hole exit.

7) SEM analysis showed that several forms of damage were present in the machined holes such as bent fibres, broken and segmented fibres, fibre impressions caused by broken fibres which couldn't escape

from the cutting zone and were forced onto the hole surfaces by the continuous rubbing and movement of the cutting tool.

8) Overall, the error in the FE model compared to experimental results found for CD and UAD did not exceed 15 %. The FE model results show a good comparison of the thrust force profiles and how it changes at different stages of the drilling process.

9) The FE model shows a better understanding of stresses and strains produced during the drilling processes. The stresses produced in the UAD are lower but spread over a larger area, whereas for the CD, higher stresses were produced and were more concentrated around the hole periphery. High strain was seen in CD compared to UAD, especially at the last aluminium sheet which contributes to exit delamination.

CRediT authorship contribution statement

Muhammad Atif: Conceptualization, Data curation, Formal analysis, Investigation, Methodology, Software, Validation, Visualization, Writing – original draft, Writing – review & editing. **Xibin Wang:** Supervision, Resources, Formal analysis, Methodology. **Lijing Xie:** Resources, Supervision, Formal analysis, Methodology, Project administration. **Khaled Giasin:** Conceptualization, Data curation, Formal analysis, Investigation, Methodology, Project administration, Resources, Supervision, Validation, Writing – original draft, Writing – review & editing. **Yuan Ma:** Investigation, Methodology, Resources. **Chulin Jiang:** Investigation, Writing – original draft, Resources. **Ugur Koklu:** Methodology, Resources, Writing – original draft, Formal analysis, Investigation. **Jos Sinke:** Resources, Writing – original draft.

Declaration of competing interest

The authors declare that they have no known competing financial interests or personal relationships that could have appeared to influence the work reported in this paper.
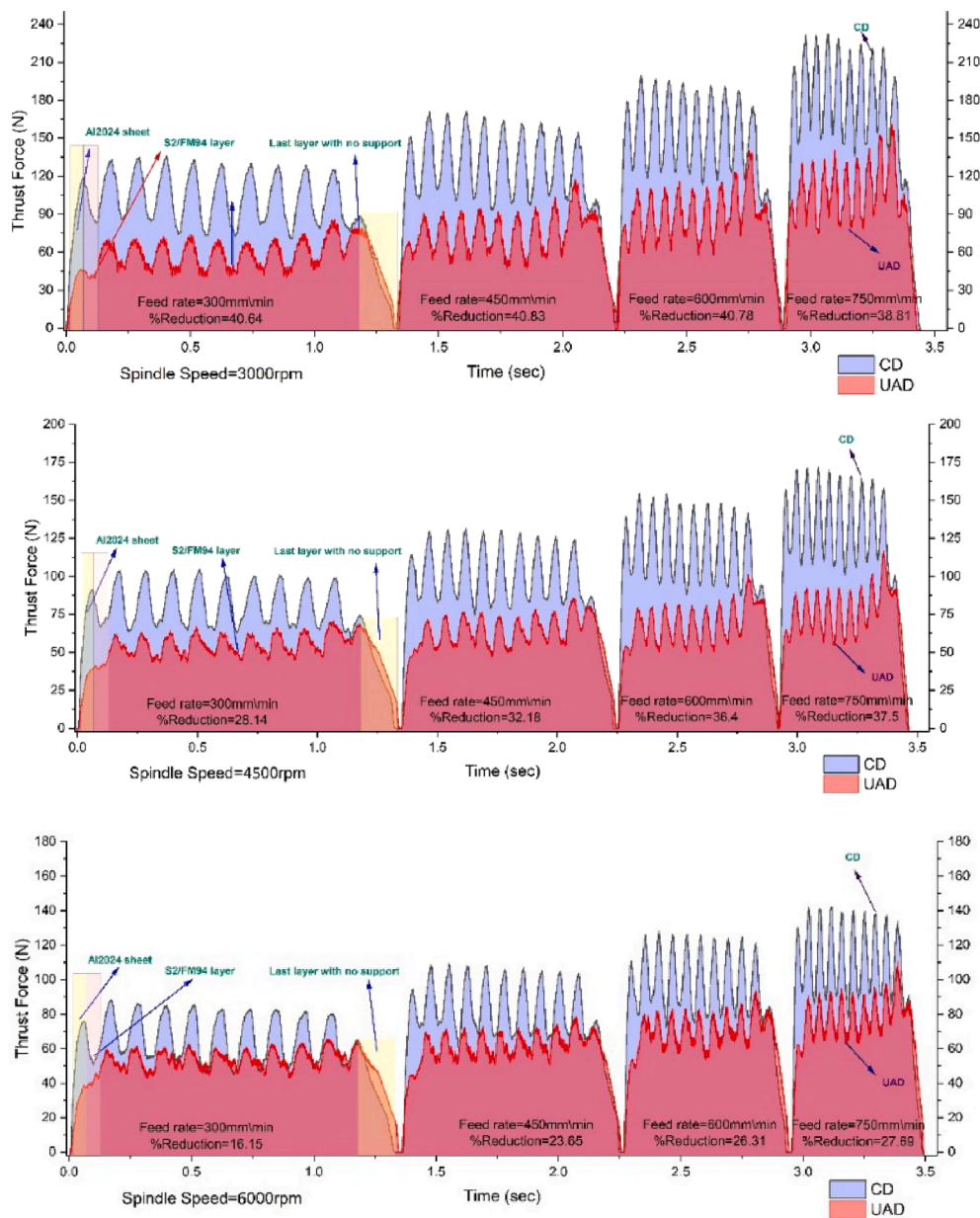
Data availability

Data will be made available on request.

Acknowledgements

Appendix A:. Thrust force profiles of CD and UAD tests at different cutting parameters

References

[1] Ad Vlot JWG. Fibre Metal Laminates: An Introduction. Kluwer Academic Publishers; 2001. doi: 10.1007/978-94-010-0995-9.

[2] Seo H. Damage tolerance and durability of GLARE laminates. Los Angeles: University of California; 2008.

[3] Sadighi M, Pärnänen T, Alderliesten RC, Sayeaftabi M, Benedictus R. Experimental and numerical investigation of metal type and thickness effects on the impact resistance of fiber metal laminates. Appl Compos Mater 2012;19(3):545–59. https://doi.org/10.1007/s10443-011-9235-6.

[4] Vlot A, Vogelesang LB, De Vries TJ. Towards application of fibre metal laminates in large aircraft. Aircr Eng Aerosp Technol 1999. https://doi.org/10.1108/00022669910303711.

[5] Maria M. Advanced composite materials of the future in aerospace industry. Incas Bullet 2013;5:139–50.

[6] Pawar OA, Gaikhe YS, Tewari A, Sundaram R, Joshi SS. Analysis of hole quality in drilling GLARE fiber metal laminates. Compos Struct 2015;123:350–65. https://doi.org/10.1016/j.compstruct.2014.12.056.

[7] Geng D, Liu Y, Shao Z, Lu Z, Cai J, Li X, et al. Delamination formation, evaluation and suppression during drilling of composite laminates: A review. Compos Struct 2019;216:168–86. https://doi.org/10.1016/j.compstruct.2019.02.099.

[8] Kim K-H, Chang-Hee C, Jeon SY, Lee K, Dornfeld D. Drilling and deburring in a single process. PROC INST MECH ENG B-J ENG MA 2003;217:1327–31. https://doi.org/10.1243/095440503322420250.

[9] Gillespie LK. Deburring precision miniature parts. Precis Eng 1979;1(4):189–98. https://doi.org/10.1016/0141-6359(79)90099-0.

[10] Choi I-H, Kim J-D. Electrochemical deburring system using electroplated CBN wheels. Int J Mach Tool Manu 1998;38(1):29–40. https://doi.org/10.1016/S0890-6955(97)00027-8.

[11] Giasin K, Ayvar-Soberanis S. An Investigation of burrs, chip formation, hole size, circularity and delamination during drilling operation of GLARE using ANOVA. Compos Struct 2017;159:745–60. https://doi.org/10.1016/j.compstruct.2016.10.015.

[12] Giasin K, Hawxwell J, Sinke J, Dhakal H, Köklü U, Brousseau E. The effect of cutting tool coating on the form and dimensional errors of machined holes in GLARE® fibre metal laminates. Int J Adv Manuf Technol 2020;107(5):2817–32. https://doi.org/10.1007/s00170-020-05211-2.

[13] Giasin K, Ayvar-Soberanis S, Hodzic A. An experimental study on drilling of unidirectional GLARE fibre metal laminates. Compos Struct 2015;133:794–808. https://doi.org/10.1016/j.compstruct.2015.08.007.

[14] Giasin K, Ayvar-Soberanis S, French T, Phadnis V. 3D finite element modelling of cutting forces in drilling fibre metal laminates and experimental hole quality analysis. Appl Compos Mater 2017;24(1):113–37. https://doi.org/10.1007/s10443-016-9517-0.

[15] Park SY, Choi WJ, Choi CH, Choi HS. Effect of drilling parameters on hole quality and delamination of hybrid GLARE laminate. Compos Struct 2018;185:684–98. https://doi.org/10.1016/j.compstruct.2017.11.073.

[16] Akula S, Bolar G. Comparative evaluation of machining processes for making holes in GLARE fiber metal laminates. Mater Today: Proc 2021;46:9126–31. https://doi.org/10.1016/j.matpr.2021.05.411.

[17] Sorrentino L, Turchetta S, Parodo G. Drilling of glare laminates: effect of cutting parameters on process forces and temperatures. Int J Adv Manuf Technol 2022;120(1):645–57. https://doi.org/10.1007/s00170-021-08612-z.

[18] Sadek A, Attia MH, Meshreki M, Shi B. Characterization and optimization of vibration-assisted drilling of fibre reinforced epoxy laminates. CIRP Ann 2013;62(1):91–4. https://doi.org/10.1016/j.cirp.2013.03.097.

[19] Linbo Z, Lijiang W, Xin W. Study on vibration drilling of fiber reinforced plastics with hybrid variation parameters method. Compos A Appl Sci Manuf 2003;34(3):237–44. https://doi.org/10.1016/S1359-835X(02)00207-5.

[20] Arul S, Vijayaraghavan L, Malhotra SK, Krishnamurthy R. The effect of vibratory drilling on hole quality in polymeric composites. Int J Mach Tool Manu 2006;46(3):252–9. https://doi.org/10.1016/j.ijmachtools.2005.05.023.

[21] Makhdum F, Phadnis VA, Roy A, Silberschmidt VV. Effect of ultrasonically-assisted drilling on carbon-fibre-reinforced plastics. J Sound Vib 2014;333(23):5939–52. https://doi.org/10.1016/j.jsv.2014.05.042.

[22] Mehbudi P, Baghlani V, Akbari J, Bushroa AR, Mardi NA. Applying ultrasonic vibration to decrease drilling-induced delamination in GFRP laminates. Procedia CIRP 2013;6:577–82. https://doi.org/10.1016/j.procir.2013.03.097.

[23] Sanda A, Arriola I, Garcia Navas V, Bengoetxea I, Gonzalo O. Ultrasonically assisted drilling of carbon fibre reinforced plastics and Ti6Al4V. J Manuf Process 2016;22:169–76. https://doi.org/10.1016/j.jmapro.2016.03.003.

[24] Wei L, Wang D. Comparative study on drilling effect between conventional drilling and ultrasonic-assisted drilling of Ti-6Al-4V/Al2024-T351 laminated material. Int J Adv Manuf Technol 2019;103(1):141–52. https://doi.org/10.1007/s00170-019-03507-6.

[25] Azarhoushang B, Akbari J. Ultrasonic-assisted drilling of Inconel 738-LC. Int J Mach Tool Manu 2007;47(7):1027–33. https://doi.org/10.1016/j.ijmachtools.2006.10.007.

[26] Shao Z, Jiang X, Li Z, Geng D, Li S, Zhang D. Feasibility study on ultrasonic-assisted drilling of CFRP/Ti stacks by single-shot under dry condition. Int J Adv Manuf Technol 2019;105(1):1259–73. https://doi.org/10.1007/s00170-019-04329-2.

[27] Hsu I, Tsao CC. Study on the effect of frequency tracing in ultrasonic-assisted drilling of titanium alloy. Int J Adv Manuf Technol 2009;43(1):127–35. https://doi.org/10.1007/s00170-008-1696-x.

[28] Li Z, Zhang D, Qin W, Geng D. Removal analyses of chip and rod in rotary ultrasonic-assisted drilling of carbon fiber-reinforced plastics using core drill.

J Reinforc Plast Compos 2016;35(15):1173–90. https://doi.org/10.1177/0731684416644510.

[29] Chen D, Chen J, Zhou H. The finite element analysis of machining characteristics of titanium alloy in ultrasonic vibration assisted machining. J Mech Sci Technol 2021;35:3601–18. https://doi.org/10.1007/s12206-021-0731-9.

[30] Lotfi M, Akbari J. Finite element simulation of ultrasonic-assisted machining: a review. Int J Adv Manuf Technol 2021;116:2777–96. https://doi.org/10.1007/s00170-021-07205-0.

[31] Phadnis VA, Makhdum F, Roy A, Silberschmidt VV. Drilling in carbon/epoxy composites: Experimental investigations and finite element implementation. Compos A Appl Sci Manuf 2013;47:41–51. https://doi.org/10.1016/j.compositesa.2012.11.020.

[32] Phadnis VA, Makhdum F, Roy A, Silberschmidt VV. Experimental and Numerical Investigations in Conventional and Ultrasonically Assisted Drilling of CFRP Laminate. Procedia CIRP 2012;1:455–9. https://doi.org/10.1016/j.procir.2012.04.081.

[33] Hocheng H, Tsao CC. The path towards delamination-free drilling of composite materials. J Mater Process Technol 2005;167(2):251–64. https://doi.org/10.1016/j.jmatprotec.2005.06.039.

[34] Hocheng H, Tsao CC. Comprehensive analysis of delamination in drilling of composite materials with various drill bits. J Mater Process Technol 2003;140(1):335–9. https://doi.org/10.1016/S0924-0136(03)00749-0.

[35] Rahme P, Moussa P, Lachaud F, Landon Y. Effect of adding a woven glass ply at the exit of the hole of CFRP laminates on delamination during drilling. Compos A Appl Sci Manuf 2020;129:105731. https://doi.org/10.1016/j.compositesa.2019.105731.

[36] Rahme P, Landon Y, Lachaud F, Piquet R, Lagarrigue P. Drilling of thick composite materials using a step gundrill. Compos A Appl Sci Manuf 2017;103:304–13. https://doi.org/10.1016/j.compositesa.2017.10.016.

[37] Giasin K, Atif M, Ma Y, Jiang C, Koklu U, Sinke J. Machining GLARE fibre metal laminates: a comparative study on drilling effect between conventional and ultrasonic-assisted drilling. Int J Adv Manuf Technol 2022;123(9):3657–72. https://doi.org/10.1007/s00170-022-10297-x.

[38] Giasin K, Hodzic A, Phadnis V, Ayvar-Soberanis S. Assessment of cutting forces and hole quality in drilling Al2024 aluminium alloy: experimental and finite element study. Int J Adv Manuf Technol 2016;87:1–21. https://doi.org/10.1007/s00170-016-8563-y.

[39] Zhang R, Han B, Li L, Zhao Z-N, Zhang Q, Zhang QC, et al. Influence of prestress on ballistic performance of bi-layer ceramic composite armors: experiments and simulations. Compos Struct 2019. https://doi.org/10.1016/j.compstruct.2019.111258.

[40] Curiel Sosa JL, Karapurath N. Delamination modelling of GLARE using the extended finite element method. Compos Sci Technol 2012;72(7):788–91. https://doi.org/10.1016/j.compscitech.2012.02.005.

[41] Simulia D. Abaqus 6.13 User's Manual. Dassault Systems, Providence, RI, 2013.

[42] Sosa JC, Karapurath N. Delamination modelling of GLARE using the extended finite element method. Compos Sci Technol 2012;72(7):788–91. https://doi.org/10.1016/j.compscitech.2012.02.005.

[43] Mohit G, Frank A, Michael F, and Galib A. Predicting Bearing Strength of Fiber Metal Laminates Via Progressive Failure Analysis. In: 52nd AIAA/ASME/ASCE/AHS/ASC Structures, Structural Dynamics and Materials Conference. 2011, American Institute of Aeronautics and Astronautics Doi: 10.2514/6.2011-2055.

[44] Seidt JD, Gilat A. Plastic deformation of 2024–T351 aluminum plate over a wide range of loading conditions. Int J Solids Struct 2013;50(10):1781–90. https://doi.org/10.1016/j.ijsolstr.2013.02.006.

[45] Zhang L, Wang X, Pei J, Zhou Y. Review of automated fibre placement and its prospects for advanced composites. J Mater Sci 2020;55(17):7121–55. https://doi.org/10.1007/s10853-019-04090-7.

[46] Dao, M, Lu L, Shen Y, Suresh S. Strength, strain-rate sensitivity and ductility of copper with nanoscale twins. 2006.

[47] Yamada H, Kami T, Mori R, Kudo T, Okada M. Strain rate dependence of material strength in AA5xxx series aluminum alloys and evaluation of their constitutive equation. Metals 2018;8:576. https://doi.org/10.3390/met8080576.

[48] Liew WY, Jie JLL, Yan LY, Dayou J, Sipaut CS, Madlan MFB. Frictional and wear behaviour of AlCrN, TiN, TiAlN single-layer coatings, and TiAlN/AlCrN, AlN/TiN nano-multilayer coatings in dry sliding. Procedia Eng 2013;68:512–7. https://doi.org/10.1016/j.proeng.2013.12.214.

[49] Cadena NL, Cue-Sampedro R, Siller HR, Arizmendi-Morquecho AM, Rivera-Solorio CI, Di-Nardo S. Study of PVD AlCrN coating for reducing carbide cutting tool deterioration in the machining of titanium alloys. Materials 2013;6(6):2143–54. https://doi.org/10.3390/ma6062143.

[50] Teimouri R, Amini S. Analytical and experimental approaches to study elastic deflection of thin strip in ultrasonic-assisted drilling process. Proc Instit Mech Eng Part E: J Process Mech Eng 2019;233(1):21–34. https://doi.org/10.1177/0954408917739453.

[51] Giasin K, Ayvar-Soberanis S. Evaluation of workpiece temperature during drilling of GLARE fiber metal laminates using infrared techniques: effect of cutting parameters. Fiber Orient Spray Mist Applicat 2016;9(8):622. https://doi.org/10.3390/ma9080622.

[52] Wilk MS, Sliwa RE. The Influence of Features of Aluminium Alloys 2024, 6061 and 7075 on the Properties of Glare-Type Composites / Wpływ Właściwości Stopów Aluminium 2024, 6061, 7075 Na Cechy Kompozytu Typu Glare. Archives of Metallurgy and Materials, 2015. 60 DOI: 10.1515/amm-2015-0496.

[53] Koklu U, Morkavuk S, Featherston C, Haddad M, Sanders D, Aamir M, et al. The effect of cryogenic machining of S2 glass fibre composite on the hole form and

dimensional tolerances. Int J Adv Manuf Technol 2021;115(1):125–40. https://doi.org/10.1007/s00170-021-07150-y.

[54] Giasin K, Ayvar-Soberanis S, Hodzic A. Evaluation of cryogenic cooling and minimum quantity lubrication effects on machining GLARE laminates using design of experiments. J Clean Prod 2016;135:533–48. https://doi.org/10.1016/j.jclepro.2016.06.098.

[55] Ma G, Kang R, Dong Z, Yin S, Bao Y, Guo D. Hole quality in longitudinal–torsional coupled ultrasonic vibration assisted drilling of carbon fiber reinforced plastics. Front Mech Eng 2020:1–9. https://doi.org/10.1007/s11465-020-0598-y.

[56] Wang D, Onawumi P, Ismail SO, Dhakal HN, Popov I, Silberschmidt VV, et al. Machinability of natural-fibre-reinforced polymer composites: Conventional vs ultrasonically-assisted machining. Compos Part A: Appl Sci 2019;119:188–95. https://doi.org/10.1016/j.compositesa.2019.01.028.

[57] Mikhailova N, Onawumi PY, Volkov G, Smirnov I, Broseghini M, Roy A, et al. Ultrasonically assisted drilling in marble. J Sound Vib 2019;460:114880. https://doi.org/10.1016/j.jsv.2019.114880.

[58] Alam K, Hassan E, Imran SH, Khan M. In-vitro analysis of forces in conventional and ultrasonically assisted drilling of bone. Bio-Med Mater Eng 2016;27(1):101–10. https://doi.org/10.3233/BME-161569.

[59] Xiao X. Interaction between micro-amplitude vibration and thrust force in ultrasonic-vibration-assisted drilling of glass-fiber-reinforced plastics. J Compos Sci 2022;7(1):4. https://doi.org/10.3390/jcs7010004.

[60] Uddin M, Basak A, Pramanik A, Singh S, Krolczyk GM, Prakash C. Evaluating hole quality in drilling of Al 6061 alloys. Materials 2018;11(12):2443. https://doi.org/10.3390/ma11122443.

[61] Onawumi PY, Roy A, Silberschmidt VV, Merson E. Ultrasonically assisted drilling of aerospace CFRP/Ti stacks. Procedia CIRP 2018;77:383–6. https://doi.org/10.1016/j.procir.2018.09.041.

[62] Giasin K. Machining fibre metal laminates and Al2024-T3 aluminium alloy. University of Sheffield; 2017.

[63] Giasin K, Ayvar-Soberanis S, Hodzic A. The effects of minimum quantity lubrication and cryogenic liquid nitrogen cooling on drilled hole quality in GLARE fibre metal laminates. Mater Des 2016;89:996–1006. https://doi.org/10.1016/j.matdes.2015.10.049.

[64] Ma G, Kang R, Dong Z, Yin S, Bao Y, Guo D. Hole quality in longitudinal–torsional coupled ultrasonic vibration assisted drilling of carbon fiber reinforced plastics. Front Mech Eng 2020;15(4):538–46. https://doi.org/10.1007/s11465-020-0598-y.

[65] Magsipoc E, Zhao Q, Grasselli G. 2D and 3D Roughness Characterization. Rock Mech Rock Eng 2020;53(3):1495–519. https://doi.org/10.1007/s00603-019-01977-4.

[66] Mittal RK, Yadav S, Singh RK. Mechanistic force and burr modeling in high-speed microdrilling of Ti6Al4V. Procedia CIRP 2017;58:329–34. https://doi.org/10.1016/j.procir.2017.03.232.

[67] Thakre AA, Soni S. Modeling of burr size in drilling of aluminum silicon carbide composites using response surface methodology. Eng Sci Technol Int J 2016;19(3):1199–205. https://doi.org/10.1016/j.jestch.2016.02.007.

[68] Dong S, Liao W, Zheng K, Liu J, Feng J. Investigation on exit burr in robotic rotary ultrasonic drilling of CFRP/aluminum stacks. Int J Mech Sci 2019;151:868–76. https://doi.org/10.1016/j.ijmecsci.2018.12.039.

[69] Giasin K, Ayvar-Soberanis S, French T, Phadnis V. 3D finite element modelling of cutting forces in drilling fibre metal laminates and experimental hole quality analysis. Appl Compos Mater 2016:1–25. https://doi.org/10.1007/s10443-016-9517-0.

[70] Isbilir O, Ghassemieh E. Finite element analysis of drilling of carbon fibre reinforced composites. Appl Compos Mater 2012;19(3):637–56. https://doi.org/10.1007/s10443-011-9224-9.